Available online at www.sciencedirect.com

Applied Energy

Journal homepage: *https://www.journals.elsevier.com/applied-energy/*

Time-delay Stability Switching Boundary Determination for DC Microgrid Clusters with the Distributed Control Framework

Chaoyu Dong[a], Qingbin Gao[b]*, Qian Xiao[a], Xiaodan Yu[a]†, Libor Pekař[c], Hongjie Jia[a]

[a] *School of Electrical and Information Engineering, Tianjin University, Tianjin, 300072, China*
[b] *Department of Mechanical Engineering, The University of Alabama, Tuscaloosa, 35487, USA*
[c] *Faculty of Applied Informatics, Tomas Bata University, Zlin, 76005, Czech Republic*

Response to Editor

Abstract

In a DC microgrid cluster, distributed DC microgrids are integrated to manage diverse and distributed energy resources. Without the reliance on a management center, the distributed control framework is capable of the cluster deployment by only adjacent collaborations. However, the communication among microgrids and the formation of dispatch signals inevitably lead to time delays, which might cause the system disorder and multiple-delay couplings. Considering these unstable effects, the lack of time-delay study challenges the cluster stability and burdens the energy application. The key contributions of this paper are the definition and detection of the time-delay stability switching boundary for the DC microgrid cluster with the distributed control framework, which reveals time delays switching the system stability and proves the delay-induced oscillation. Through the established time-delay model and the proposed method based on the cluster treatment of characteristic roots, the explicit time-delay stability switching boundary is detected in the delay space, which forms a determination flow of five stages: 1) system initialization: according to the cluster parameter values, the established time-delay model is initialized; 2) space transformation: applying the space mapping and the rationalization, the Sylvester resultant is constructed in the spectral delay space; 3) spectral boundary sketch: in uniformly divided blocks, spectral boundaries are found from the resultant; 4) crossing root calculation: with the spectral boundaries, crossing roots are calculated solving the characteristic equation; 5) boundary determination: back-mapping the spectral boundaries with the crossing roots, the overall boundary is presented. Comprehensive case studies are performed to study the time-delay stability switching boundary and to validate the proposed approach. The boundary existence and feature demonstrate the time-delay effect. Furthermore, the classified stable areas are revealed as well as the relevant strategies for the stability enhancement.

Keywords: time-delay stability switching boundary, DC microgrid cluster, distributed control, multiple delays

* Corresponding author. Tel.: +1 (475) 200-0351; fax: +1 (562) 985-1503.
E-mail address: qingbin.gao@gmail.com
* Corresponding author. Tel.: +022-27892811; fax: +022-27892811.
E-mail address: yuxd@tju.edu.cn;

The short version of the paper was presented at REM2017, October 18-20, Tianjin, China. This paper is a substantial extension of the short version of the conference paper

Nomenclature

$\boldsymbol{A}_0$	non-delay coefficient	TDSSB	time-delay stability switching boundary
$\boldsymbol{A}_{\tau p}$	time-delay coefficient for τ_p	$\boldsymbol{\tau}$	time-delay vector
$\boldsymbol{A}$	adjacency matrix	$\boldsymbol{\tau}_{KB}$	point on the KB
$\boldsymbol{\alpha}$	integral gain vector	$\boldsymbol{\tau}_{OB}$	point on the OB
α_k	integral gain of k^{th} DC microgrid	$\boldsymbol{u}$	control vector of the secondary layer
CTCR	cluster treatment of characteristic roots	u_k	control signal generated by consensus control
CE	characteristic equation	V^*	nominal DC voltage
$\boldsymbol{D}$	in-degree matrix	v_{Kr}	reflection point on the Kr
FWM	free-weighting matrix	v_{Or}	reflection point on the Or
i	imaginary part of Sylvester resultant	$\boldsymbol{v}_p$	reflection point on the spectral delay space
i_k	output current of k^{th} DC microgrid	v_{droop}	voltage signal generated by droop control
j_p	derivation number for τ_p	v_{DC}	DC bus voltage
JI	Jensen inequality	ω_c	crossing root on the complex plane
KB	kernel boundary	$\boldsymbol{w}_1$	weighting vector for voltage comparison
Kr	kernel reflection	$\boldsymbol{w}_2$	weighting vector for consensus comparison
$\boldsymbol{M}$	Sylvester resultant matrix	w_{1k}	voltage comparison weight of k^{th} DC microgrid
M_k	droop gain of k^{th} DC microgrid	w_{2k}	consensus comparison weight of k^{th} DC microgrid
OB	offspring boundary	x_{1k}	voltage deviation of k^{th} DC microgrid
Or	offspring reflection	x_{2k}	consensus deviation of k^{th} DC microgrid
R_k	line resistance of k^{th} DC microgrid	$\boldsymbol{x}$	deviation vector
r	real part of Sylvester resultant	z_p	tangent substitution variable
τ_p	time delay of the p^{th} channel		

1. Introduction

1.1. Motivation

With the CO_2 emissions and the adverse environmental effects, the traditional fossil fuel is facing a potential crisis of exhaustion and a great curse of pollution. Stimulated by the expectation of beautiful environment and the development of energy conversion [1], dispersive renewable energy sources undertake an unprecedented penetration in both the supply and customer sides. During the transition to a low carbon, green and sustainable society, microgrids provide a promising solution for the integration of distributed energy resources, such as photovoltaics, geothermal and solar heat, wind turbines, microturbines, and various energy storage systems [2]. As a natural and simple solution for utilizing electric power, the development of DC microgrids moves towards a new stage for integrating the renewable energy source and loads. By virtue of DC microgrids, the natural DC outputs from the solar energy can be conveniently supplied to the DC loads like electric vehicles without AC conversions [3]. In the absence of the reactive power and frequency [4], DC microgrids also stay away from many issues such as inrush currents and synchronization. Hence, DC microgrids have emerged as the effective way to upgrade the energy application and evolution.

Despite those merits brought by the DC microgrids, the intermittency of renewable energy and the individual capacity of a single microgrid make the system reliability vulnerable. Once the power output in one microgrid is not able to satisfy the load demand, the load shedding would be inescapable, which may even lead to cascading failures [5]. In order to improve the reliability of a single microgrid, the microgrid

cluster provides an available solution by the connection of distributed units. Through the cloud-based approach [6], multiple DC microgrids can be effectively connected in a meshed network topology. Unaware of the current cluster state and other flows, the proposed oblivious routing algorithm is competent to solve the optimal power flow problem, while managing congestion and mitigating power losses [7]. With the coordination of different energy sources in multiple microgrids, it is not only easy to achieve the power balance [8] but also beneficial to equalize the utilization factors of different devices [9]. In this way, multiple microgrids can help each other and extend their lifespans during various situations.

The control framework for the clustering of multiple microgrids can be classified into centralized, decentralized, and distributed categories. In a centralized control system, there exists at least one control center collecting the data from all the microgrids [10]. After the extraction of operating states from those data, control center generates command signals and sends them back to each microgrid. The centralized framework requires the establishment and maintenance of a high bandwidth network between the control center and every individual microgrid [11]. Because of the high reliance on the communication network and the central controller, the cluster system easily suffers from any failure or accident in these two parts. To improve the system reliability, the decentralized control framework embeds an individual controller in each microgrid [12]. Without the information exchange, every individual controller fulfills its own operation objective. This is a more reliable structure that the control center and the communication network are completely avoided [13]. But this full autonomy is injurious to the system benefit and flexibility due to the lack of global information. As all the microgrids only care about their own operation, the cooperation like the energy sharing is difficult to achieve.

To overcome this problem, the distributed control framework hybridizes the centralized and decentralized structures as a whole. Besides the microgrid [14], the applications of the distributed control framework can be found in other energy systems like the building energy systems [15], electric vehicle systems [16], etc. The distributed control framework can usually be divided into two layers [17]. In the primary control layer, decentralized control strategies such as the droop control are employed to guarantee the independent operation of each microgrid. The secondary control layer then adjusts the individual operation from the cluster aspect. Through the coordination between only neighboring microgrids, the distributed control can achieve the global target as well as the autonomy of every microgrid [18]. For the accomplishment of the reliability and flexibility simultaneously, the distributed control framework provides a viable option for the management of DC microgrid cluster. However, the distributed control framework still requires the communication network to accomplish the global objective. Because the mutual communication and the signal processing take time to finish, the induced time delay becomes an inevitable factor for the distributed control framework.

1.2. Related work

As the open communication network has the high potential for being integrated with future distributed energy systems, the network-induced delays would become obvious due to the limited bandwidth of end-users [19]. It was reported that the dynamics of microgrid currents take much longer time to decay because of the time-delay effect [20]. The authors in [21] suggest that the communication with shorter

time delay is preferable in the microgrid control to protect the system from the possible disorder. Besides those bad effects, the time-delay issue may be more complex and more serious owing to the existence of multiple delays. With two identical delays, the system frequency tends to oscillate [22] without careful configuration. The control algorithms become ineffective taking non-uniform time-varying delays into account [23]. Although those undesirable effects have been mentioned in those studies, accurate time-delay stability analyses have not been carried out yet. Besides, there are few articles devoted to the abovementioned time-delay issue for the DC microgrid cluster in the literature. The lack of the formulated delay model, analysis, and the explicit stability switching information all beset the stability assessment of the microgrid clusters.

For the stability analysis of time delays, the Lyapunov-based method and the eigenvalue-based method are representative. Through the construction of Lyapunov functionals and the deployment of the linear matrix inequality [24], the Lyapunov-based method derives sufficient stability criteria for time-delay systems [25]. The approximate maximum delay without breaking the system stability can then be calculated by various criteria [26]. Although the development of the Lyapunov-based method is speedy, the demerit of conservativeness posts constraints in the stability analysis [27]. The lack of a unified and systematic approach predisposes most Lyapunov functionals to extreme difficulties for construction. Moreover, various inequalities during the derivation process aggravate the inaccuracy by the introduction of scaling errors [28]. Therefore, those conservative results are not accurate to provide the factual time-delay boundary for DC microgrid clusters.

By contrast, eigenvalue-based methods determine the time-delay margin by computing purely imaginary roots of characteristic equations, which can deliver the more exact results. In [29], Padé approximants were used to evaluate the transcendental terms in the characteristic equation. The crossing root was then calculated with the corresponding time delays. Through the construction of the Schur-Cohn-Fujiwara matrix and the eigenvalues of the Hamiltonian matrix, [30] calculated the delay margin for the linear delay systems. But both of them only reckoned the minimum margin, which is ineffective to determine the complete information of all stability switching boundaries. To overcome this problem, the cluster treatment of characteristic roots (CTCR) [31] were proposed to establish the relationship between the time-delay space and the spectral delay space. Employing the root-clustering feature, the concepts of “kernel” and “offspring” are also introduced, which imparts the complete portrait of the possible imaginary root crossings of time-delay systems.

The difference comparisons of those methods can be presented from three aspects:

1) Objective. CTCR technique aims to find out all the time delays switching the system stability, which can provide complete stability switching information caused by the time delays. However, other methods like [29] only calculate the minimum delay value that a time-delay system can endure. Without complete stability information related to time-delay, very strict time-delay constraints might be introduced during the microgrid cooperation, which would lead to the unnecessary cost and control;

2) Application range. For the employment of existing methods in [30], the time-delay values in different communication channels should be assumed the same, .i.e., the suitability of single-delay analyses. However, CTCR is carried out in the time-delay space, which is capable of single-delay and multiple-delay analyses simultaneously;

3) Accuracy. As the constructed results in CTCR is the necessary and sufficient condition for the time-delay stability judgment, critical time delays can be determined accurately. But Lyapunov-based methods like [26] can only provide sufficient stability criteria for time-d ation results are conservative.

Response to Reviewer 6

Notwithstanding those merits of the CTCR, whether it is suitable for the time-delay analysis of DC microgrid cluster and how to implement this technique have not been investigated so far.

1.3. Contribution

This paper presents a systemic analysis approach including the time-delay model, analysis method, and stability switching investigation for the DC microgrid cluster with the distributed control framework. With the droop control in the primary layer and the consensus control in the secondary layer, a distributed control framework is utilized to manage the power dispatch and the DC voltage of the cluster. Based on this demonstrated DC microgrid cluster, a global analysis model is then built to incorporate the time delays in the coordination network. In order to figure out all the stability switching scenario, the time-delay stability switching boundary (TDSSB) is defined mathematically for the DC microgrid cluster, which reveals the explicit transition from stability to instability as well as a theoretical proof for the oscillation phenomenon induced by the time delays. Considering the coupling of the variable crossing roots and the delay components in the TDSSB definition, the CTCR technique is employed to convert the issue in the time-delay space to the spectral delay space, based on which we design a streamline of five stages for the TDSSB determination. With the system initialization and the space transformation as the first two stages, the rationalized Sylvester resultant can be constructed. After that, the spectral boundary sketch and the crossing root calculation are implemented to search the critical points in the spectral delay space and the relevant oscillating frequencies. According to the relationship between these two spaces, the objective of TDSSB determination can be achieved in the last stage, which assembles the overall time-delay points switching the stability of the DC microgrid cluster.

Four major contributions of this paper are summarized as below.

1) TDSSB is defined mathematically for the DC microgrid cluster with the distributed control framework and proved as an oscillation source;

2) A time-delay stability analysis model for the DC microgrid cluster with the distributed control framework is derived, which facilitates model-based investigations for the global stability of the cluster;

3) Based on the time-delay model, a systematic method is proposed to determine the TDSSB of the DC microgrid cluster by utilizing the CTCR. By the designed implementation flow of five stages, the TDSSB panorama can be presented effectively;

4) From the single-delay scenario to the multiple-delay one, the accurate TDSSB is determined and validated for the DC microgrid cluster with the distributed control framework. With the help of the explicit TDSSB, stable areas can be divided advancing stability tactics for the microgrid cluster.

1.4. Organization

The rest of this paper is organized as follows. Section 2 specifies the derivation and analyses of the time-delay model for the DC microgrid cluster with the distributed control framework. In Section 3, a

CTCR-based method is proposed to determine the accurate TDSSB as well as a designed streamline of five stages. Case studies are presented in Section 4 where three different scenarios are carefully investigated. Based on the determined TDSSB, two strategies are also raised to improve the time-delay stability. Besides, the accuracy of the proposed method is indicated comparing with existing methods. Finally, we present the summary and conclusion of this work in Section 5.

2. Time-delay model for the DC microgrid cluster with the distributed control framework

In this study, the DC microgrid cluster with the distributed control framework is depicted in Fig. 1. With the DC microgrid cluster of Fig. 1, the distributed DC microgrid 1,…, DC microgrid *k*,…, DC microgrid *n* are aggregated to a relatively larger system. During the operation of this cluster, the energies can be reasonably dispatched among multiple microgrids. It is beneficial not only for the proper employment of diverse energy sources from the solar panels and batteries, but also for the satisfaction of various requirements from time-variant loads.

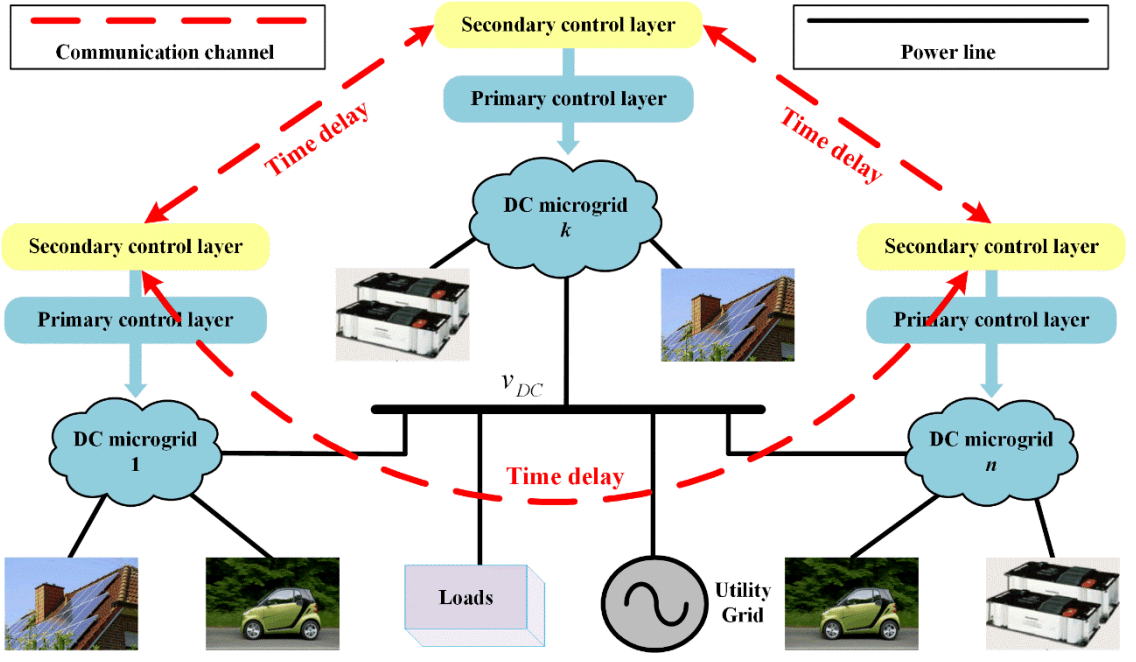

Fig. 1. The DC microgrid cluster with the distributed control framework.

As shown in Fig. 1, the distributed control framework is made up of two control layers to manage the DC microgrid cluster. In the primary control layer, the control objective is designed to guarantee the fundamental operation of every microgrid. Measuring only the local information like the output currents and the terminal voltages, all the microgrids are capable of independent operations, which benefits the reliability of the whole system. Meanwhile, the secondary control layer utilizes the sparse network to adjust the control signals. Through only the neighboring interactions, the global control objective like the preservation of the common DC voltage can be achieved without a central controller. However, the distance between microgrids is not always close enough, which would make the time delays in the communication channels (represented by red dashed lines in Fig. 1) unavoidable. Indeed, there may exist multiple time delays in different exchange channels. Once any coupling happens among those multiple

delays, unrevealed risks might occur and even affect the stability of the whole cluster. For the stability investigation via a model-based approach, the distributed control framework with the droop control and the consensus control is utilized as an instance.

2.1. DC microgrid cluster with the primary droop control

In order to control the DC microgrid cluster in a decentralized approach, the droop control is widely employed for the power sharing [3]. According to the output current i_k and the droop gains M_k, the voltage reference is generated for each microgrid

$$v_{droop}(t) = V^* - M_k i_k(t) \tag{1}$$

where V^* is the nominal bus voltage of the common DC bus.

Considering the line resistance between the microgrid and the common bus, the DC bus voltage v_{DC} is obtained as

$$v_{DC}(t) = v_{droop}(t) - R_k i_k(t) \tag{2}$$

where R_k, k=1,2,…,n, is the line resistance, respectively. From (1)-(2), the real-time v_{DC} is expressed as

$$v_{DC}(t) = V^* - (M_k + R_k) i_k(t) \tag{3}$$

As the DC microgrids are connected parallel to the common DC bus shown in Fig. 2, (3) holds for all the microgrids, which implies $(M_k + R_k) i_k(t) = (M_l + R_l) i_l(t), \forall k, l$. Thus, the output currents of all the DC microgrids can be pre-designed proportionally by setting the droop gains much larger than the line resistances. However, this control strategy will cause the inevitable voltage deviation between v_{DC} and V^* in (3). As the DC bus is the main concern for the microgrid cluster, the bus voltage must be compensated by proper strategies.

2.2. Time-delay in the secondary consensus control

Without the global information exchange, the consensus control strategy provides a powerful strategy only employing the adjacent cooperation. In Fig. 2, the consensus control in [17] is demonstrated here. Two kinds of deviation information are collected to generate the control signal $u_k(t)$ for the voltage recovery. With the measured bus voltage, the voltage deviation $x_{1k}(t)$ is obtained in the k^{th} DC microgrid

$$x_{1k}(t) = V^* - v_{DC}(t) \tag{4}$$

Besides the voltage deviation, neighboring control signals are compared to keep the power ratio determined by the droop control, which forms the consensus deviation

$$x_{2k}(t) = \sum_{l \in N_k} [u_l(t - \tau_{lk}) - u_k(t)] \tag{5}$$

where N_k is the neighborhood set of the k^{th} microgrid, τ_{kl} is the time delay during the message exchange between k^{th} DC microgrid and l^{th} DC microgrid. Denoting $\boldsymbol{u}(t) = [u_1(t), \ldots, u_k(t), \ldots, u_n(t)]^T$, the vector of consensus errors $\boldsymbol{x}_2(t) = [\boldsymbol{x}_{21}(t), \ldots, \boldsymbol{x}_{2k}(t), \ldots, \boldsymbol{x}_{2n}(t)]^T$ can be obtained from (5)

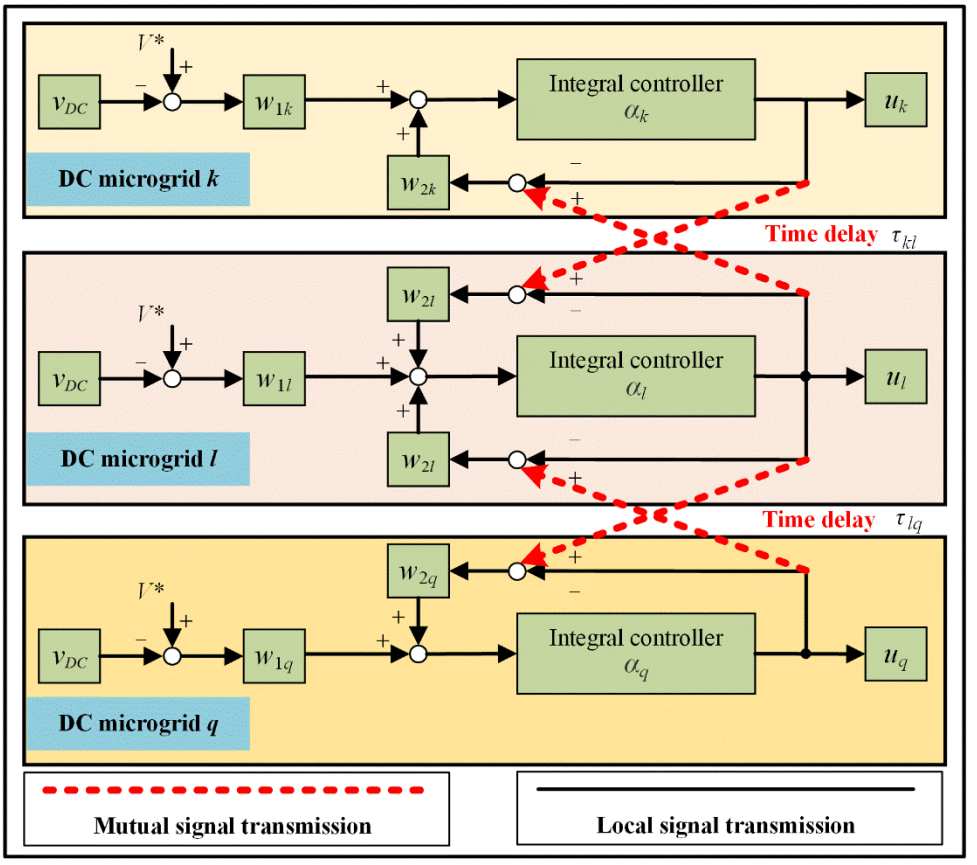

Fig. 2. The secondary consensus control for the DC microgrid cluster.

(The secondary control signals u_k/ u_l/ u_q are formed through the embedded integral controllers α_k/ α_l/ α_q based on the weighted voltage deviations via w_{1k}/ w_{1l}/ w_{1q} and the weighted consensus deviations via w_{2k}/ w_{2l}/ w_{2q}. Time delays τ_{kl} and τ_{lq} occur during the neighboring interactions among k^{th}/l^{th}/q^{th} DC microgrids.)

$$\boldsymbol{x}_2(t) = \sum_{p=1}^{m} \boldsymbol{A}_p \boldsymbol{u}(t-\tau_p) - \boldsymbol{D}\boldsymbol{u}(t) \tag{6}$$

where $\sum \boldsymbol{A}_p = \boldsymbol{A}$, p=1,2,…,m, is the index of each channel, $\boldsymbol{A} = [a_{kl}] \in \mathbf{R}^{n\times n}$ is the adjacency matrix, the element $a_{kl} = a_{lk} = 1$ if $l \in N_k$; otherwise, $a_{kl} = a_{lk} = 0$; $\boldsymbol{A}_p = [a_{pkl}] \in \mathbf{R}^{n\times n}$, $a_{pkl} = a_{plk} = 1$, $\tau_p = \tau_{kl} = \tau_{lk}$, if (k,l) forms the channel p; otherwise, $a_{pkl} = a_{plk} = 0$; $\boldsymbol{D} \in \mathbf{R}^{n\times n}$ is the diagonal in-degree matrix with $\boldsymbol{D}_{kk} = \sum_{l=1}^{n} a_{kl}$. If all the delay values are 0, v_{DC} can recovered to V^* with pre-designed droop gains when (4)-(5) converge to 0. But the communication and the signal process always induce time delays. Hence, the derivation of a time-delay stability analysis model for the DC microgrid cluster becomes necessary.

2.3. Time-delay model for the global stability analysis

In order to achieve the voltage restoration without affecting the power allocation, the consensus control output $\boldsymbol{u}(t)$ is added for the voltage reference adjustment in the droop control. According to (4) and the adjusted reference in (3), the real-time $\boldsymbol{x}_1(t) = [\boldsymbol{x}_{11}(t),\ldots,\boldsymbol{x}_{1k}(t),\ldots,\boldsymbol{x}_{1n}(t)]^T$ becomes

$$\boldsymbol{x}_1(t) = \boldsymbol{D}_{RM}\boldsymbol{i}(t) - \boldsymbol{u}(t) \tag{7}$$

where $\boldsymbol{D}_{RM} = diag\{R_k + M_k\}$, $\boldsymbol{i}(t) = [i_1(t),\ldots,i_k(t),\ldots,i_n(t)]^T$.

For the further derivation of the system model, the common resistance load is taken as an example. Assuming R to be the equivalent resistance of all loads, the relevant load current $i_L(t)$ can be obtained

$$i_L(t) = v_{DC}(t) / R \tag{8}$$

According to the Kirchhoff's Circuit Law [32], $i_L(t)$ equals to the sum of $i_k(t)$, k=1,2,…, n

$$i_L(t) = \sum_{k=1}^{n} i_k(t) \tag{9}$$

Combining (8) and (9), the DC bus voltage is expressed by the load resistance R and the branch current of each microgrid

$$v_{DC}(t) = R\sum_{k=1}^{n} i_k(t) \tag{10}$$

The relationship between the microgrid currents and control signals is then derived from (10) and (3)

$$\boldsymbol{i}(t) = \boldsymbol{Z}^{-1}V^*\boldsymbol{I}_{n\times 1} + \boldsymbol{Z}^{-1}\boldsymbol{u}(t) \tag{11}$$

where $\boldsymbol{Z} = \boldsymbol{D}_{RM} + R\boldsymbol{I}_{n\times n}$, $\boldsymbol{D}_{RM} = diag\{R_k + M_k\}$, $\boldsymbol{I}_{n\times n}$ is the $n\times n$ matrix with all elements being 1, $\boldsymbol{I}_{n\times 1}$ is the $n\times 1$ vector with all elements are 1.

Based on (11) and (7), $\boldsymbol{x}_1(t)$ can be reflected by $\boldsymbol{u}(t)$

$$\boldsymbol{x}_1(t) = \boldsymbol{D}_{RM}\boldsymbol{Z}^{-1}V^* \cdot \boldsymbol{I}_{n\times 1} - R\boldsymbol{I}_{n\times n}\boldsymbol{Z}^{-1}\boldsymbol{u}(t) \tag{12}$$

Denoting $\boldsymbol{w}_1 = diag\{w_{11},\cdots,w_{k1},\cdots,w_{n1}\}$ and $\boldsymbol{w}_2 = diag\{w_{12},\cdots,w_{k2},\cdots,w_{n2}\}$ as the weighting vectors for $\boldsymbol{x}_1(t)$ and $\boldsymbol{x}_2(t)$ respectively, the summation of deviation $\boldsymbol{x}(t)$ can be written as

$$\boldsymbol{x}(t) = \boldsymbol{w}_1\boldsymbol{x}_1(t) + \boldsymbol{w}_2\boldsymbol{x}_2(t) \tag{13}$$

Substituting (12) and (6) into (13) yields

$$\boldsymbol{x}(t) = \boldsymbol{w}_1[\boldsymbol{D}_{RM}\boldsymbol{Z}^{-1}V^* \cdot \boldsymbol{I}_{n\times 1} - R\boldsymbol{I}_{n\times n}\boldsymbol{Z}^{-1}\boldsymbol{u}(t)] + \boldsymbol{w}_2\sum_{p=1}^{m}\boldsymbol{A}_p\boldsymbol{u}(t-\tau_p) - \boldsymbol{w}_2\boldsymbol{D}\boldsymbol{u}(t) \tag{14}$$

The dynamics of the cluster can then be obtained by the derivative of (13) with respect to t

$$\frac{d\boldsymbol{x}(t)}{dt} = -(\boldsymbol{w}_1R\boldsymbol{I}_{n\times n}\boldsymbol{Z}^{-1} + \boldsymbol{w}_2\boldsymbol{D})\frac{d\boldsymbol{u}(t)}{dt} + \boldsymbol{w}_2\sum_{p=1}^{m}\boldsymbol{A}_p\frac{d\boldsymbol{u}(t-\tau_p)}{dt} \tag{15}$$

As the secondary consensus control utilizes the integral component to eliminate the total error in Fig. 2, the derivatives of the control vectors $\boldsymbol{u}(t-\tau_p)$, $\boldsymbol{u}(t)$ are $\boldsymbol{\alpha}\boldsymbol{x}(t-\tau_p)$ and $\boldsymbol{\alpha}\boldsymbol{x}(t)$ respectively, where $\boldsymbol{\alpha} = diag\{\alpha_1,\cdots,\alpha_k,\cdots,\alpha_n\}$, α_k, k=1,2,…,n, are the integral gains. Therefore, (15) can be rewritten as

$$\frac{d\boldsymbol{x}(t)}{dt} = \boldsymbol{A}_0\boldsymbol{x}(t) + \sum_{p=1}^{m}\boldsymbol{A}_{\tau p}\boldsymbol{x}(t-\tau_p) \tag{16}$$

where $\boldsymbol{A}_0 = -(\boldsymbol{w}_1R\boldsymbol{I}_{n\times n}\boldsymbol{Z}^{-1} + \boldsymbol{w}_2\boldsymbol{D})\boldsymbol{\alpha}$, $\boldsymbol{A}_{\tau p} = \boldsymbol{w}_2\boldsymbol{A}_p\boldsymbol{\alpha}$. Different from a small signal stability model close to a certain operation point, (16) provides a time-delay model for the global stability analysis of DC microgrid cluster without the needed linearization procedure.

3. Time-delay stability switching boundary (TDSSB) determination

As the stable operation is the main concern for the cluster, it is important to keep the whole system far away from any unstable state caused by the time-delay part in the model (16). In this section, the TDSSB is defined in the time-delay space revealing all the stability switching delays. A TDSSB determination method and the corresponding implementation flow are then proposed for the DC microgrid cluster.

3.1. TDSSB definition

The characteristic equation of the DC microgrid cluster (16) is

$$\mathrm{CE}(s,\boldsymbol{\tau}) = \det\left(s\boldsymbol{I} - \boldsymbol{A}_0 - \sum_{p=1}^{m} \boldsymbol{A}_{\tau p} e^{-\tau_p s}\right) \tag{17}$$

where s is the Laplace operator, $\boldsymbol{\tau} = [\tau_1,...,\tau_p,...,\tau_m]^T \in \mathbf{R}^m$ indicates a point in the time-delay space composed of m time-delay components.

With all the eigenvalues of the matrix $\boldsymbol{A}_0 + \sum_{p=1}^{m} \boldsymbol{A}_{\tau p}$ designed on the left side of the complex plane, the system stability can be guaranteed in the ideal zero-delay scenario, i.e., $\boldsymbol{\tau} = \mathbf{0}$. But the fact that $\boldsymbol{\tau} \neq \mathbf{0}$ during the practical operation makes the transcendental terms in (17) non-constants, which becomes uncertain risks for the cluster stability.

In order to sort out all the time-delay points switching the DC microgrid cluster stability, the time-delay stability switching boundary (TDSSB) is defined in the time-delay space

$$\mathrm{TDSSB} = \{\boldsymbol{\tau} \mid \det\left(i\omega_c \boldsymbol{I} - \boldsymbol{A}_0 - \sum_{p=1}^{m} \boldsymbol{A}_{\tau p} e^{-i\tau_p \omega_c}\right) = 0, \boldsymbol{\tau} \in \mathbf{R}^{n+}, \omega_c \in \mathrm{R}^+\} \tag{18}$$

where $i\omega_c$ is the crossing root in the complex plane. In the definition above, any point on the TDSSB is associated with at least one purely imaginary root of the system characteristic equation. It can be seen from (18) that two constraints of $\boldsymbol{\tau} \in \mathbf{R}^{n+}$ and $\omega_c \in \mathrm{R}^+$ have been posted for the TDSSB. During the operation of the DC microgrid cluster, each component of the time-delay points is positive, which makes $\boldsymbol{\tau} \in \mathbf{R}^{n+}$. In terms of the other constraint $\omega_c \in \mathrm{R}^+$, a theorem is given as follows.

Theorem 1: The time delays τ_p, p=1,2,…,m, do not induce the crossing root through the origin for the DC microgrid cluster model (16).

Proof: This is a proof by contradiction. If the time delays τ_p, p=1,2,…,m, induce the crossing root through the origin, there exists at least one $\boldsymbol{\tau}$ associated with $\omega_c = 0$. In other words, λ=0 would become an eigenvalue of $\boldsymbol{A}_0 + \sum_{p} \boldsymbol{A}_{\tau p}$. But all the eigenvalues $\boldsymbol{A}_0 + \sum_{p} \boldsymbol{A}_{\tau p}$ have been designed negative for $\boldsymbol{\tau} = \mathbf{0}$ in the time-delay space. Here comes the contradiction. Q.E.D.

On the basis of this theorem, only $\omega_c \neq 0$ needs to be considered for the TDSSB, which means that time delays are potential sources for oscillations. According to the conjugation of imaginary roots, the range of ω_c is further narrowed to R^{n+}. Therefore, the defined TDSSB includes all the essential time-

delay points despite these conditions. As the exponential term $e^{-i\tau_p\omega_c}$ has the period of 2π concerning the product of τ_p and ω_c, the defined TDSSB can be categorized into two sub-boundaries:

Kernel Boundary (KB): The boundary that consists of all the points $\boldsymbol{\tau} \in \mathbf{R}^{n+}$ corresponding to $i\omega_c$ occurrence and satisfies the constraint $0 < \tau_p\omega_c < 2\pi$, p=1,2,…, m. This constraint entails that the points on the KB display the smallest delay compositions.

Offspring Boundary (OB): The boundary is derived from the KB by the following point-wise transformation

$$(\tau_1 \pm 2\pi j_1 / \omega_c, ..., \tau_p \pm 2\pi j_p / \omega_c, ..., \tau_m \pm 2\pi j_m / \omega_c) \tag{19}$$

where j_p=1,2,…,∞, are not zeroes simultaneously. It can be seen from (19) that any point on the KB results in ∞^n (n-dimensional infinity) OB over the identical crossing root $i\omega_c$.

Instead of determining infinite number of boundaries, this classification reveals that keeping track of the KB is more effective and efficient. However, the coupling of two variables, i.e., $\boldsymbol{\tau}$ and $i\omega_c$ in the characteristic equation (18), forms the main challenge for the determination of TDSSB. Moreover, the nonlinear transformation (19) has the variable ω_c as the denominator, which hampers the analysis.

3.2. Spectral delay space mapping

In order to settle those two problems, the spectral delay space is introduced by the technique of cluster treatment of characteristic roots (CTCR) [31]. The conditional mapping rule is given as follows:

If a delay set $\boldsymbol{\tau} \in \mathbf{R}^{n+}$ induces the imaginary root $i\omega_c$, then $\boldsymbol{\nu} = \boldsymbol{\tau}\omega_c$ forms a point in the spectral delay space. On the contrary, the left points in the time-delay space are not presented.

According to this mapping rule, the representation of KB in the spectral delay space is denoted as the kernel reflection (Kr)

$$\mathrm{Kr} = \{\boldsymbol{\nu}_{Kr} \mid \boldsymbol{\tau}_{KB} \in \mathrm{KB}, 0 < \boldsymbol{\nu}_{Kr}^T \boldsymbol{e}_p < 2\pi, p = 1,2,...,m\} \tag{20}$$

where $\boldsymbol{e}_p = [0,\ldots,1,\ldots,0]^T$ is a unit vector, $\boldsymbol{e}_p(p,1) = 1$. Similarly, the OB projection is called the offspring reflection (Or)

$$\mathrm{Or} = \{\boldsymbol{\nu}_{Or} \mid \boldsymbol{\tau}_{OB} \in \mathrm{OB}, \boldsymbol{\nu}_{Or}^T \boldsymbol{e}_p > 2\pi, p = 1,2,...,m\} \tag{21}$$

On the basis of the mapping rule above, the characteristic equation of the DC microgrid with the distributed control framework can then be rewritten in the spectral delay space as

$$\mathrm{CE}(\omega_c, \boldsymbol{\nu}) = \det\left(i\omega_c \boldsymbol{I} - \boldsymbol{A}_0 - \sum_{p=1}^{m} \boldsymbol{A}_{\tau p} e^{-i\nu_p}\right) \tag{22}$$

Remark:

According to (20)-(22), there are three merits of the spectral delay space mapping:

1) Numerical simplification: Without searching in the space of the infinite length on each edge, only Kr needs to be determined in the limited space;

2) Linearized Transformation: The transition from the Kr to the Or is easily fulfilled by stacking the copies of the Kr, which avoids the undesirable distortion due to the point-wise nonlinear transformation;

3) Boundary isolation: The whole space can be evenly divided into small blocks with the lengths of 2π, which isolates all the boundaries from each other.

3.3. TDSSB determination

As the existence of exponential terms still causes the troubles for solving (22), they are replaced with the Euler's formula

$$e^{-iv_p} = \cos(v_p) - i\sin(v_p),\ p = 1,2,...,m \tag{23}$$

Denoting $z_p = \tan(v_p / 2)$, (23) is then rewritten by the half-angle tangent

$$e^{-iv_p} = \frac{1-z_p^2}{1+z_p^2} - i\frac{2z_p}{1+z_p^2} \tag{24}$$

By substituting (24) into (23), the characteristic equation is rationalized as

$$\mathrm{CE}(\omega_c, z_1, \ldots, z_m) = \det\left[i\omega_c \boldsymbol{I} - \boldsymbol{A}_0 - \sum_{p=1}^{m} \boldsymbol{A}_{\tau p}\left(\frac{1-z_p^2}{1+z_p^2} - i\frac{2z_p}{1+z_p^2}\right)\right] \tag{25}$$

For different crossing roots, any solution needs to make both real and imaginary parts of (25) vanish

$$\mathrm{Re}[\mathrm{CE}(\omega_c, z_1, \ldots, z_m)] = 0 \tag{26}$$

$$\mathrm{Im}[\mathrm{CE}(\omega_c, z_1, \ldots, z_m)] = 0 \tag{27}$$

To guarantee these two equations established under any crossing root $i\omega_c$, the Sylvester matrix [33] is formed to be singular

$$|\boldsymbol{M}| = \begin{vmatrix} r_h(z_1,...,z_m) & \cdots & r_0(z_1,...,z_m) & 0 & \cdots & 0 & 0 \\ 0 & r_h(z_1,...,z_m) & \cdots & r_0(z_1,...,z_m) & 0 & \cdots & 0 \\ \vdots & \ddots & \ddots & \ddots & \ddots & \ddots & \vdots \\ 0 & \cdots & 0 & 0 & r_h(z_1,...,z_m) & \cdots & r_0(z_1,...,z_m) \\ i_l(z_1,...,z_m) & \cdots & i_0(z_1,...,z_m) & 0 & \cdots & 0 & 0 \\ 0 & i_l(z_1,...,z_m) & \cdots & i_0(z_1,...,z_m) & 0 & \cdots & 0 \\ \vdots & \ddots & \ddots & \ddots & \ddots & \ddots & \vdots \\ 0 & \cdots & 0 & 0 & i_l(z_1,...,z_m) & \cdots & i_0(z_1,...,z_m) \end{vmatrix} = 0 \tag{28}$$

where $r_h(z_1,\ldots,z_m),...,r_0(z_1,\ldots,z_m)$ are the real-part coefficients, h is the degree of (26); $i_l(z_1,\ldots,z_m),...,i_0(z_1,\ldots,z_m)$ are the imaginary-part coefficients, l is the degree of (27).

Depending on the relationship between the kernel reflection and the offspring ones, the derivation rule from the Kr to the Or is as follows

$$\mathrm{Or} = \{\boldsymbol{v}_{Or} \mid \boldsymbol{v}_{Kr} \in \mathrm{Kr}, \boldsymbol{v}_{Or} = \boldsymbol{v}_{Kr} + 2\pi j_p \boldsymbol{e}_p\} \tag{29}$$

where j_p, $p = 1,2,...,m$ are the derivation number. Their values cannot be 0 at the same time.

While an infinite number of Ors are generated from the derivation rule (29), the corresponding crossing roots remained the same compared to those regarding the Kr. With the knowledge of all the crucial $\tilde{z}_p$ from (28), ω_c becomes the only variable, which results in the equation below

$$\det\left[i\omega_c \boldsymbol{I} - \boldsymbol{A}_0 - \sum_{p=1}^{m} \boldsymbol{A}_{\tau p}\left(\frac{1-\tilde{z}_p^2}{1+\tilde{z}_p^2} - i\frac{2\tilde{z}_p}{1+\tilde{z}_p^2}\right)\right] = 0 \tag{30}$$

The kernel boundary and the offspring boundary of TDSSB are then obtained by the inverse transformations below

$$\mathrm{KB} = \{\boldsymbol{\tau}_{KB} \mid \boldsymbol{\nu}_{Kr} \in \mathrm{Kr}, \boldsymbol{\tau}_{KB} = \boldsymbol{\nu}_{Kr} / \omega_c\} \tag{31}$$

$$\mathrm{OB} = \{\boldsymbol{\tau}_{OB} \mid \boldsymbol{\nu}_{Or} \in \mathrm{Or}, \boldsymbol{\tau}_{OB} = \boldsymbol{\nu}_{Or} / \omega_c\} \tag{32}$$

3.4. Implementation flow for the TDSSB determination

In light of Section 3.1-3.3, an implementation flow of five stages is designed to determinate the TDSSB for the DC microgrid cluster.

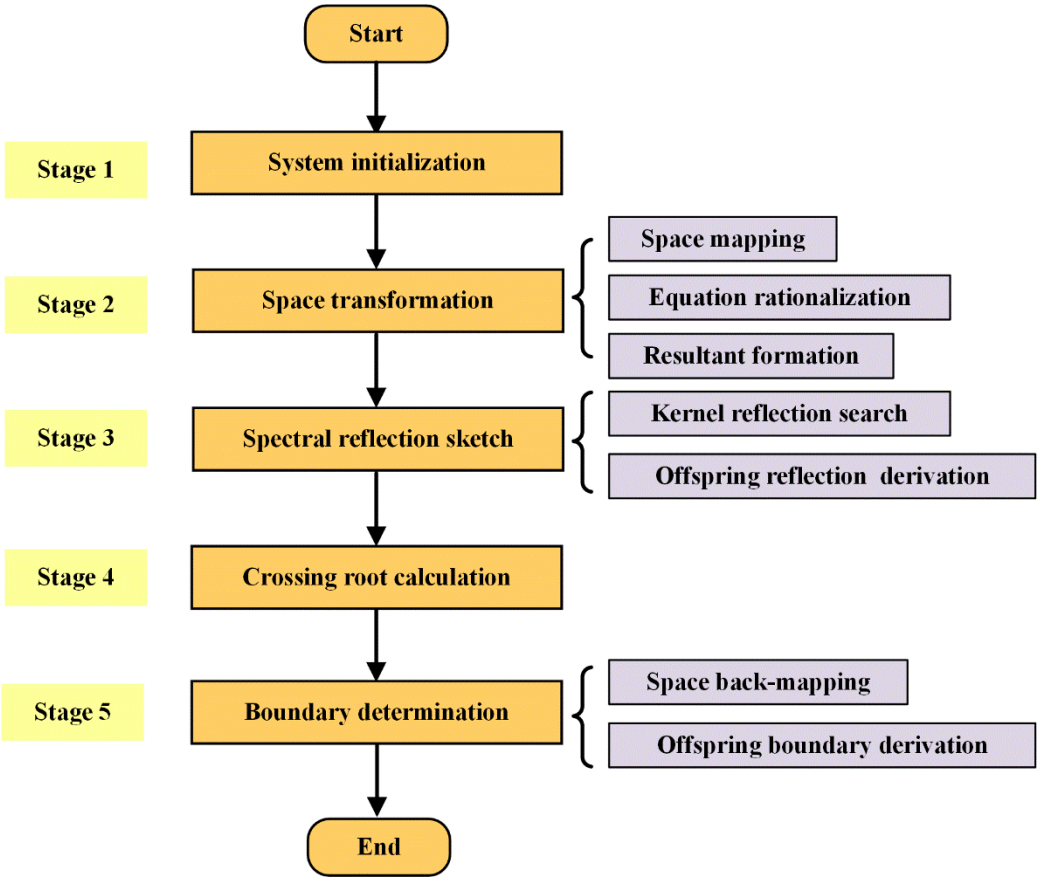

Fig. 3. Implementation flow for the TDSSB determination of the DC microgrid cluster.

Each stage in the flowchart in Fig. 3 is detailed as follows.

Stage 1: System initialization.

With the parameters of the DC microgrid cluster, the coefficients in the time-delay model (16) and the derivation number j_p are initialized.

Stage 2: Space transformation.

a) Space mapping. Introducing $\boldsymbol{\nu} = \boldsymbol{\tau}\omega_c$, the characteristic equation (22) is obtained in the spectral delay space mapped from the time-delay space;

b) Equation rationalization. To eliminate the exponential terms, the half-angle tangent substitution is employed to form (25);

c) Resultant formation. Extracting the real-part coefficients and imaginary-part coefficients from the equation rationalization, the Sylvester resultant in (28) is constructed;

Stage 3: Spectral boundary sketch.

a) Kernel reflection search. Within 2π length on each side, critical points are solved rendering $\boldsymbol{M}$=0;

b) Offspring reflection derivation. On the basis of the derivation rule in (29) and j_p, Ors are derived quantitatively duplicating the Kr;

Stage 4: Crossing root calculation.

All the crossing roots are calculated solving (30) as well as the oscillating frequencies dividing by 2π;

Stage 5: Boundary determination.

a) Space back-mapping. The KB of the DC microgrid cluster is obtained in the time-delay space with the inverse transformation rule (31).

b) Offspring boundary derivation. Referring to (32), the OB is derived by the points on the Or.

These five stages determine the complete TDSSB, which will be validated in the next section.

4. Case studies

4.1. System description and parameter values

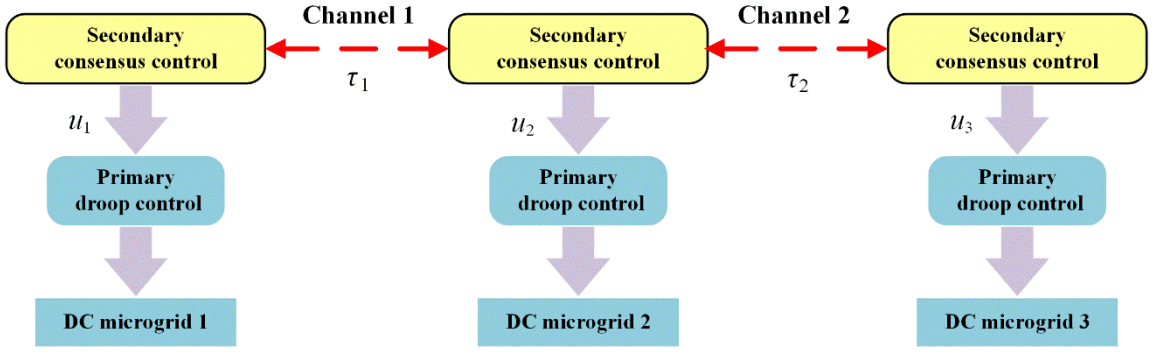

Fig. 4. The DC microgrid cluster with three DC microgrids.

For the TDSSB determination and the stability analysis, a DC microgrid cluster in Fig. 4 is employed as a demonstration. The system parameters are displayed in Table 1. The low voltage level 400V and the line résistance 0.05Ω are set for DC microgrids. The droop gain M_k represents the power-sharing ratio among the different DC microgrids. The identical power allocation is adopted in this study. The ability of voltage restoration is reflected by the integral gain α_k. The voltage comparison weight w_{1k} indicates the receiver of the voltage deviation information. The second DC microgrid is set as the receiver here. The consensus comparison weight w_{2k} indicates the collaborators in this cluster. During this illustration, all the DC microgrids would collaborate to guarantee the cluster stability. The equivalent load resistance of the DC microgrid cluster is set as 16Ω. It can be seen from Fig. 4 that two communication channels are considered in this cluster, which induces the time delays τ_1 and τ_2, respectively.

Table 1. System parameters.

Parameter	Symbol	DC microgrid 1	DC microgrid 2	DC microgrid 3
Nominal voltage	V^* (V)	400	400	400
Line resistance	R_k (Ω)	0.05	0.05	0.05
Droop gain	M_k	1	1	1
Integral gain	α_k	10	10	10
Voltage comparison weight	w_{1k}	0	1	0
Consensus comparison weight	w_{2k}	1	1	1

According to the communication network in Fig. 4, the adjacency matrix of the DC microgrid cluster is

$$\boldsymbol{A} = \begin{bmatrix} 0 & 1 & 0 \\ 1 & 0 & 1 \\ 0 & 1 & 0 \end{bmatrix} \tag{33}$$

To illustrate the TDSSB of the DC microgrid cluster with the distributed control framework, three scenarios are considered and investigated.

Scenario 1 (Non-delay scenario): the time delays in the Channel 1 and Channel 2 of the DC microgrid cluster are assumed to be 0, i.e., $\tau_1 = \tau_2 = 0$.

Scenario 2 (Single-delay scenario): the time delays in the Channel 1 and Channel 2 of the DC microgrid cluster are the identical, i.e., $\tau_1 = \tau_2 = \tau$.

Scenario 3 (Multiple-delay scenario): the time delays in the Channel 1 and Channel 2 of the DC microgrid cluster are different from each other, i.e., $\tau_1 \neq \tau_2$.

The mathematical simulations are implemented using Matlab 2015b. The computational platform is on an Intel(R) Core(TM) i3 2.53GHz personal computer with 6G memory.

4.2. Non-delay scenario

In the non-delay scenario, the time-delay model is reduced to a conventional linear model. As $\tau_1 = \tau_2 = 0$, the system dynamic is represented by a non-delay matrix $\tilde{\boldsymbol{A}}_0$

$$\tilde{\boldsymbol{A}}_0 = \begin{bmatrix} -10 & 10 & 0 \\ 6.738 & -23.262 & 6.738 \\ 0 & 10 & -10 \end{bmatrix} \tag{34}$$

The eigenvalues of $\tilde{\boldsymbol{A}}_0$ are listed in Table 2. As shown in Table 2, the three eigenvalues λ_1, λ_2, λ_3 of the DC microgrid cluster are negative real values. Therefore, the cluster is stable under the external disturbances. Besides, the system presents no oscillations as all the eigenvalues are real.

Table 2. The eigenvalues of the non-delay scenario.

Name	Symbol	Value
Eigenvalue 1	λ_1	-30
Eigenvalue 2	λ_2	-10
Eigenvalue 3	λ_3	-3.262

The DC bus variation is shown in Fig. 5 triggering a small voltage disturbance at t=5s. According to the bus curve in Fig. 5, the system voltage of the DC microgrid cluster can be effectually protected by the distributed control framework. During 0s-5s, v_{DC} operates stably at 400V. When the disturbance occurs at 5s, the DC bus voltage is quickly restored from 399.9V to 400V within 1.5s. It is also clear that the v_{DC} is monotonously recovered without any oscillations after the voltage drop. Hence, the cluster stability is well guaranteed in the non-delay scenario.

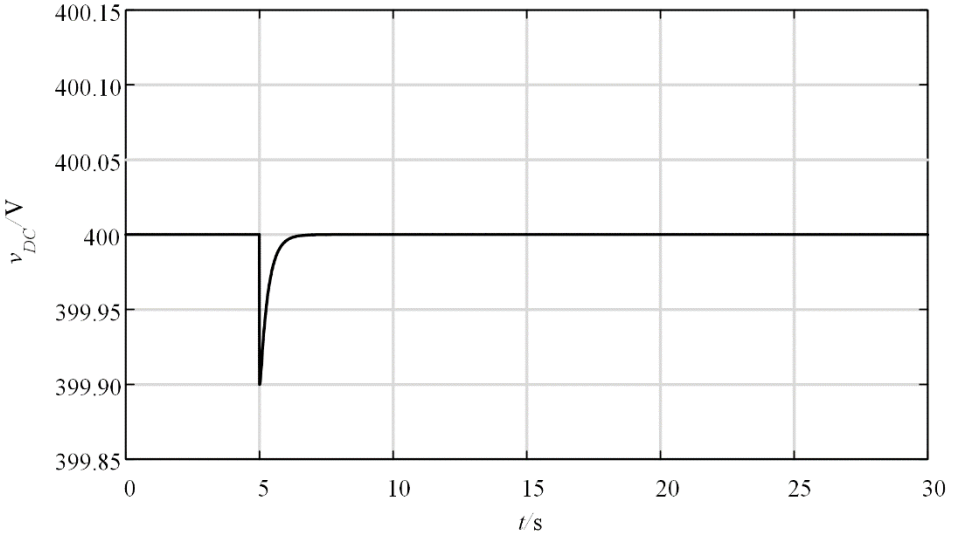

Fig. 5. DC bus voltage variation in the non-delay scenario.

4.3. Single-delay scenario

During the secondary consensus control, the control signals of neighboring DC microgrids are compared to restore the voltage maintaining the power assignment. For the comparison with the non-delay scenario, the TDSSB with the identical delay value is first analysed by the proposed method in Section 3. The implementation process is illustrated as follows.

Stage 1: System initialization.

Setting the derivation number j_p=8. The non-delay and time-delay coefficients in (16) are as follows

$$\bar{\boldsymbol{A}}_0 = \begin{bmatrix} -10 & 0 & 0 \\ -3.26 & -23.26 & -3.26 \\ 0 & 0 & -10 \end{bmatrix}, \ \bar{\boldsymbol{A}}_\tau = \begin{bmatrix} 0 & 10 & 0 \\ 10 & 0 & 10 \\ 0 & 10 & 0 \end{bmatrix} \tag{35}$$

The matrix $\tilde{\boldsymbol{A}}_0$ in the non-delay scenario has been separated into $\bar{\boldsymbol{A}}_0$ and $\bar{\boldsymbol{A}}_\tau$ in (35). The eigenvalues of these two matrices are recorded in Table 3.

Table 3. The eigenvalues of the non-delay and time-delay coefficients.

Coefficients	Eigenvalue 1	Eigenvalue 2	Eigenvalue 3
$\bar{\boldsymbol{A}}_0$	-23.262	-10	-10
$\bar{\boldsymbol{A}}_\tau$	-14.142	0	14.142

Although a time-delay coefficient has been extracted from $\tilde{\boldsymbol{A}}_0$, the eigenvalues of these two matrices

are still real as shown in Table 3. Different from the non-delay scenario, the separated $\bar{\boldsymbol{A}}_\tau$ has an unstable eigenvalue 14.142 and an eigenvalue 0, which forms the coefficient of the time-delay part.

Stage 2: Space transformation.

a) Space mapping. Through the substitution of $v = \tau\omega_c$, the characteristic equation is transformed to the spectral delay space

$$\mathrm{CE}(\omega_c, v) = \det\left(i\omega_c \boldsymbol{I}_{3\times3} - \bar{\boldsymbol{A}}_0 - \bar{\boldsymbol{A}}_\tau e^{-iv}\right) \tag{36}$$

The mapped (36) in the spectral delay space provides a simple approach to cope with the characteristic equation. Combing the two variables τ and ω_c into the variable *v*, the difficulty in determining TDSSB has been eliminated.

b) Equation rationalization. In order to eliminate the transcendental term e^{-iv}, (36) is rewritten via the half-angle tangent substitution

$$\mathrm{CE}(\omega_c, z) = \det\left[i\omega_c \boldsymbol{I}_{3\times3} - \bar{\boldsymbol{A}}_0 - \bar{\boldsymbol{A}}_\tau\left(\frac{1-z^2}{1+z^2} - i\frac{2z}{1+z^2}\right)\right] \tag{37}$$

It can be seen from (37) that the exponential component has vanished. On the basis of the rationalized equation, the time-delay problem has been simplified to a polynomial one.

c) Resultant formation. With the real-part coefficients $r_3(z)$, $r_2(z)$, $r_1(z)$, $r_0(z)$ and the imaginary-part coefficients $i_3(z)$, $i_2(z)$, $i_1(z)$, $i_0(z)$ of (37), the corresponding Sylvester resultant $\boldsymbol{M}$ is constructed

$$\boldsymbol{M} = \begin{vmatrix} r_3(z) & r_2(z) & r_1(z) & r_0(z) & 0 & 0 \\ 0 & r_3(z) & r_2(z) & r_1(z) & r_0(z) & 0 \\ 0 & 0 & r_3(z) & r_2(z) & r_1(z) & r_0(z) \\ i_3(z) & i_2(z) & i_1(z) & i_0(z) & 0 & 0 \\ 0 & i_3(z) & i_2(z) & i_1(z) & i_0(z) & 0 \\ 0 & 0 & i_3(z) & i_2(z) & i_1(z) & i_0(z) \end{vmatrix} \tag{38}$$

The matrix in (38) has the dimension of 6×6, which provides an effective tool to decouple the variables ω_c and *z*. For different imaginary roots of the characteristic equation, the real and the imaginary parts must be 0 simultaneously, which makes a zero resultant $\boldsymbol{M}$.

Stage 3: Spectral boundary sketch.

a) Kernel reflection search. According to the relationship between *z* and *v*, the variable *z* in (38) is replaced with *v*. The minimum interval (0, 2π) in the spectral delay space is evenly scanned to find out the critical point $v_{Kr} = 2.78$. Since there is only one critical point in the range of (0, 2π) for the single-delay system, this point constitutes the Kr in the spectral delay space.

b) Offspring reflection derivation. With the Kr and the derivation rule in (29), Ors are plotted in Fig. 6.

It can be seen from Fig. 6 that there are one Kr point and nine Or points in the interval of (0, 18π). With the derivation number j_p, 8 black points are found out within (2π, 18π), which are all associated with the same crossing root.

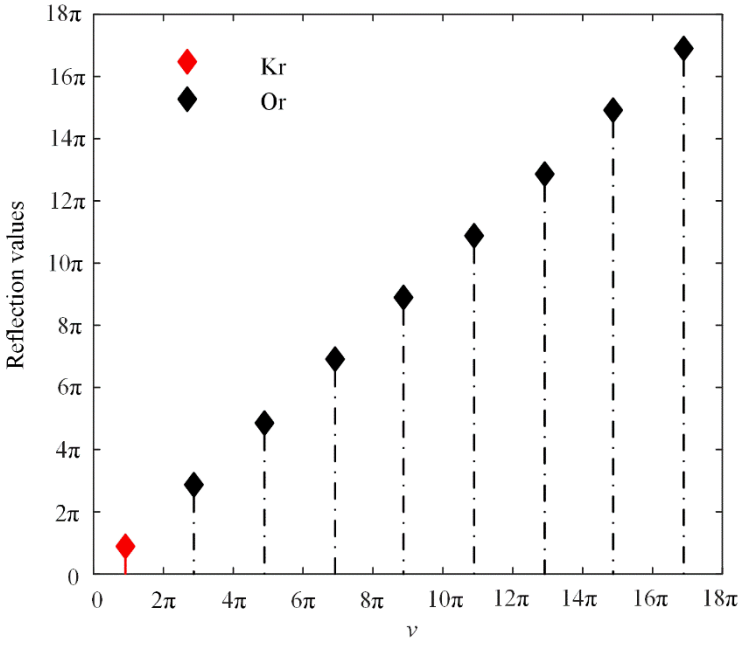

Fig. 6. The reflection values in the spectral delay space.

Stage 4: Crossing root calculation. According to the only point $v_{Kr} = 2.78$ of the Kr, the crossing root $i\omega_c = 4.67i$ is obtained solving the characteristic equation (30). This intriguing result indicates that the characteristic roots of the DC microgrid cluster periodically cross the imaginary axis at only two conjugate points $\pm 4.67i$. The corresponding oscillating frequency is 0.74Hz. During the growing of v in the spectral delay space, the stability switching times can be counted by $2(j_p + 1)$.

Stage 5: TDSSB determination.

a) Space back-mapping. With the inverse transformation rule, the KB point of the DC microgrid cluster is calculated in the time-delay space as

$$\tau_{KB} = v_{KB} / \omega_c = 0.59\text{s} \tag{39}$$

b) Offspring boundary derivation. Because there exists only one essential ω_c value, the OB points are evenly located along the time-delay axis. The coordinates of KB and the derived OB are listed in Table 4.

Table 4. The coordinates of TDSSB in the time-delay space.

	KB	OB 1	OB 2	OB 3	OB 4	OB 5	OB 6	OB 7	OB 8
τ_1	0.59	1.94	3.28	4.63	5.97	7.32	8.66	10.00	11.35
τ_2	0.59	1.94	3.28	4.63	5.97	7.32	8.66	10.00	11.35

The uniform difference for the distance between neighboring points is 1.90s in Table 4. Since 0.59s is the minimum time-delay value of the determined TDSSB, the DC voltage variation under $\tau = 0.59$s is shown in Fig. 7 to verify the proposed method.

When the value of the time delay increases, the oscillations of the DC bus become larger in magnitude from Fig. 7. Compared with the smooth curve in Fig. 5 for the non-delay scenario, the monotonous voltage variation has been broken by the delayed control signals. If τ is smaller than the minimum value of TDSSB, i.e., 0.59s, the voltage oscillation will fade with the elapse of time. Once the time delay

reaches the 0.59s, the equal amplitude oscillation will happen, which means that the system damping has disappeared due to the delay. The DC microgrid cluster will then switch to an unstable state beyond that point. For the cluster stability, the delay value should be smaller than 0.59s in this scenario.

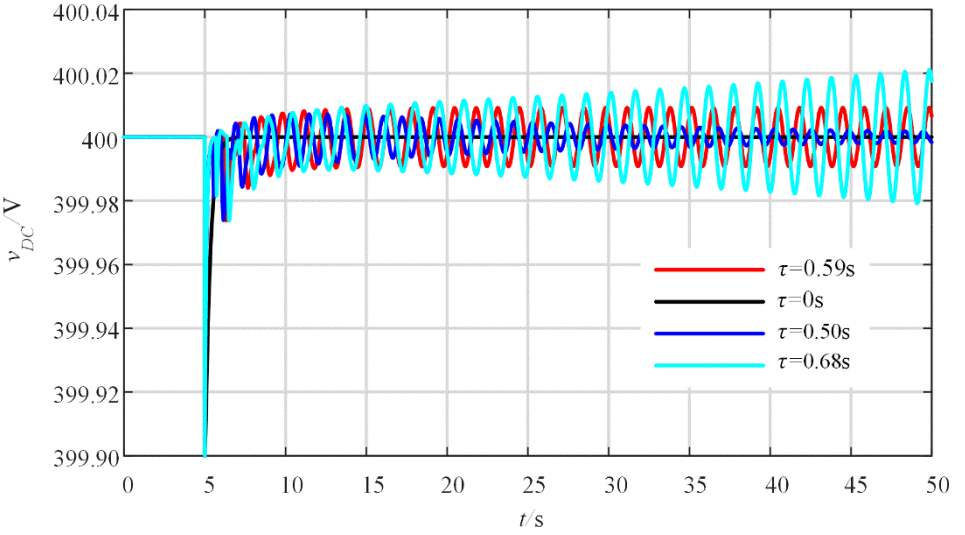

Fig. 7. DC bus voltage variations under different time-delay values.

4.4. Multiple-delay scenario

The investigation in Section 4.3 is based on the assumption that different communication channels are contaminated by an identical time delay, which is ideal for the real-time operation. In this section, the TDSSB is determined in a more general and realistic scenario considering different delay values.

Similar to the two scenarios before, the non-delay and time-delay coefficients are established

$$\boldsymbol{A}_0 = \begin{bmatrix} -10 & 0 & 0 \\ -3.26 & -23.26 & -3.26 \\ 0 & 0 & -10 \end{bmatrix},\ \boldsymbol{A}_{\tau 1} = \begin{bmatrix} 0 & 10 & 0 \\ 10 & 0 & 0 \\ 0 & 0 & 0 \end{bmatrix},\ \boldsymbol{A}_{\tau 2} = \begin{bmatrix} 0 & 0 & 0 \\ 0 & 0 & 10 \\ 0 & 10 & 0 \end{bmatrix} \tag{40}$$

The non-delay coefficients are the same as the ones in Section 4.3 and Section 4.4, while the time-delay coefficients are different. As the time delays in the Channel 1 and Channel 2 are different, the $\bar{\boldsymbol{A}}_\tau$ in the singular-delay scenario is separated into $\boldsymbol{A}_{\tau 1}$ and $\boldsymbol{A}_{\tau 2}$ in (40). According to the eigenvalues listed in Table 5, $\boldsymbol{A}_{\tau 1}$ and $\boldsymbol{A}_{\tau 2}$ have identical eigenvalues. But the spectral norms of these three matrices, i.e., their maximum eigenvalues here, satisfy $\|\boldsymbol{A}_{\tau 1}\|_2 = \|\boldsymbol{A}_{\tau 2}\|_2 < \|\bar{\boldsymbol{A}}_\tau\|_2$. It means that the individual coupling of $\boldsymbol{A}_{\tau 1}$ and τ_1 (or $\boldsymbol{A}_{\tau 2}$ and τ_2) is not as strong as that in the single-delay scenario.

Table 5. The eigenvalues of the non-delay and time-delay coefficients.

Coefficients	Eigenvalue 1	Eigenvalue 2	Eigenvalue 3
$\boldsymbol{A}_0$	-23.262	-10	-10
$\boldsymbol{A}_{\tau 1}$	-10	0	10
$\boldsymbol{A}_{\tau 2}$	-10	0	10

Following the same stages in Section 4.3, the Sylvester resultant is formed in the spectral delay space

$$\boldsymbol{M}=\begin{vmatrix} r_3(z_1,z_2) & r_2(z_1,z_2) & r_1(z_1,z_2) & r_0(z_1,z_2) & 0 & 0 \\ 0 & r_3(z_1,z_2) & r_2(z_1,z_2) & r_1(z_1,z_2) & r_0(z_1,z_2) & 0 \\ 0 & 0 & r_3(z_1,z_2) & r_2(z_1,z_2) & r_1(z_1,z_2) & r_0(z_1,z_2) \\ i_3(z_1,z_2) & i_2(z_1,z_2) & i_1(z_1,z_2) & i_0(z_1,z_2) & 0 & 0 \\ 0 & i_3(z_1,z_2) & i_2(z_1,z_2) & i_1(z_1,z_2) & i_0(z_1,z_2) & 0 \\ 0 & 0 & i_3(z_1,z_2) & i_2(z_1,z_2) & i_1(z_1,z_2) & i_0(z_1,z_2) \end{vmatrix} \tag{41}$$

where $r_3(z_1,z_2)$,…, $r_0(z_1,z_2)$ are the real-part coefficients, $i_3(z_1,z_2)$,…, $i_0(z_1,z_2)$ are the imaginary-part coefficients. With the solved 216 critical points making $\boldsymbol{M}$=0, the kernel reflection is assembled in Fig. 8.

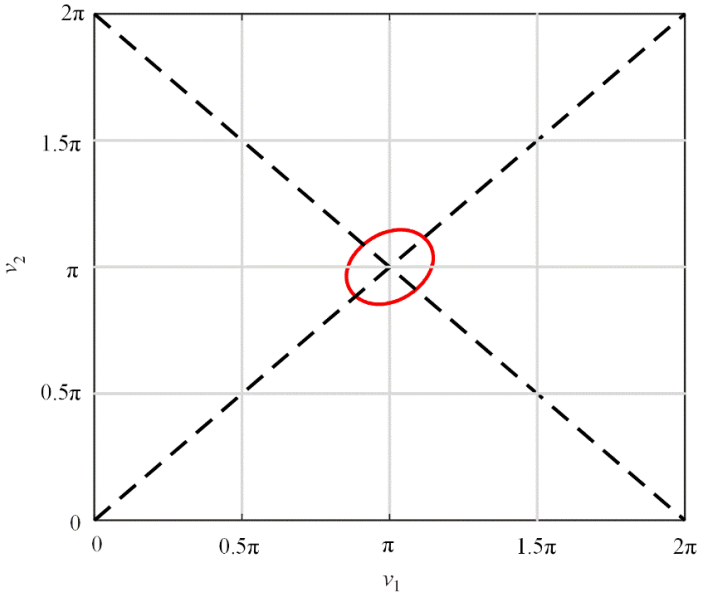

Fig. 8. The kernel reflection in the spectral delay space.

In Fig. 8, the red oval-like curve is the kernel reflection in the square region with the length 2π×2π. Crossing the two dashed diagonals, Kr locates at the regional center. Although the shape of Kr is not a circle, it can be seen that the boundary is symmetric with respect to the two diagonals of the square.

According to the period of 2π in the spectral delay space, the offspring reflections are derived by copying the Kr. The derived Ors along three directions are depicted in Fig. 9 (a)-(c).

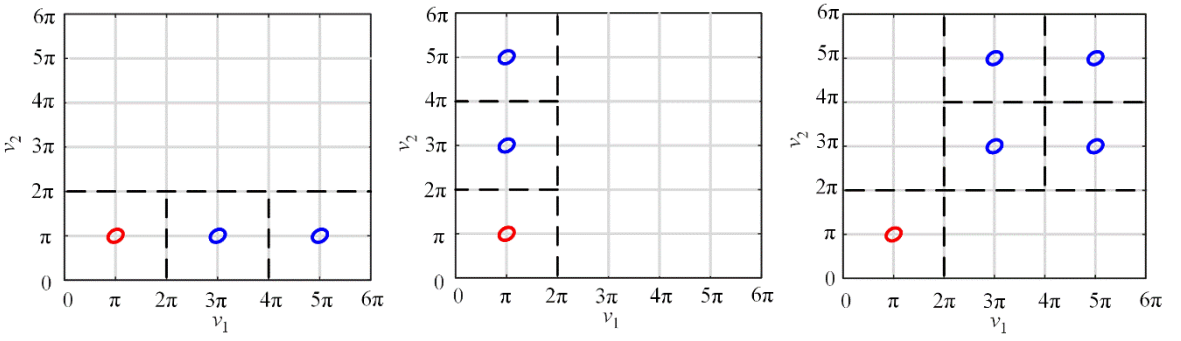

(a) Ors along the v_1 direction (b) Ors along the v_2 direction (c) Ors along the (v_1, v_2) direction

Fig. 9. The offspring reflections along three directions. (Red line: kernel reflection; blue line: offspring reflection)

From Fig. 9 (a)-(c), the mapped boundaries in the spectral delay space are shown clearly. Along the three directions, the Kr is translated to various Ors. The whole shape of all the boundaries is symmetrical along the diagonal. Even if an infinite number of offspring reflections can be derived with the 2π period, the corresponding purely imaginary roots remain unchanged. Therefore, all the $i\omega_c$ can be determined only by the kernel reflection.

Based on kernel reflection, all the crossing imaginary roots are calculated by the characteristic equation. The values of ω_c are shown in Fig. 10, where the horizontal ordinate n_S is the point indication on Kr.

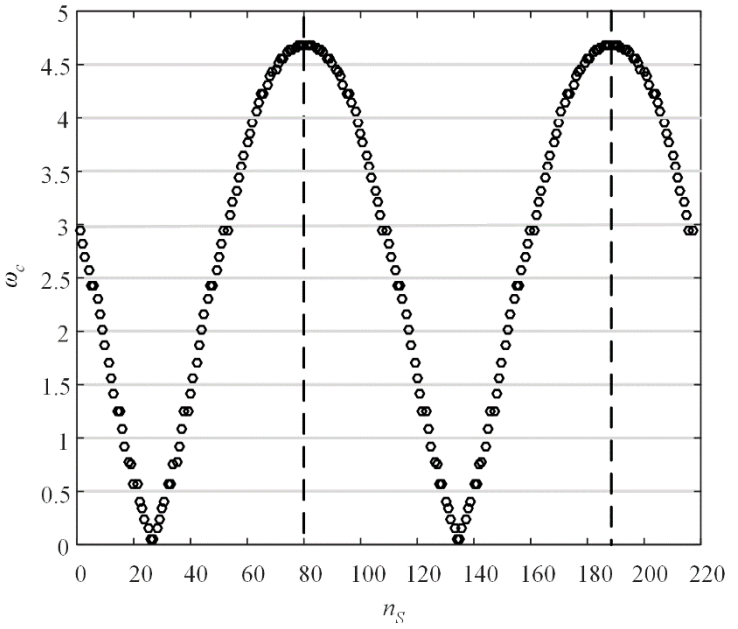

Fig. 10. The ω_c values of crossing root

As can be seen from Fig. 10, all the crossing roots are distributed within the range of [0.043, 4.67]. The radius of this range, i.e., 4.67, is just equal to the size of the crossing root in Section 4.3, which generates the maximum oscillating frequency 0.74Hz. The whole shape is similar to a sinusoidal (or cosinusoidal) function. Since all the imaginary roots exist in pairs, there are 108 pairs of $\pm\omega_c i$ for the DC microgrid cluster with the distributed control framework. According to the symmetry of Fig. 10 along the vertical dashed lines, the number of different pairs is only 54. The crossing root pair of the maximum amplitude is $\pm 4.68i$, while the pair of the minimum amplitude is $\pm 0.043i$.

The kernel boundary of the DC microgrid cluster is then back-mapped from the kernel reflection. As seen from Fig. 11, the KB is a radial curve in the time-delay space. The circular dot A (0.59, 0.59) is coincident with the TDSSB value determined in the single-delay scenario, which is the closest point to the origin. Since the smallest $\|\boldsymbol{\tau}\|_2$ causes the maximum oscillating frequency, this identical delay value in different channels should be strictly avoided. A1-A3 are three points close to KB as shown in Fig. 11. The voltage waveforms for these three points are shown in Fig. 12.

With the growing value of τ_2, A1-A3 crosses the kernel boundary vertically. The stability switching of the DC microgrid cluster is A2 with $\tau_1 = 3.00\text{s}$ and $\tau_2 = 2.50\text{s}$. As clearly seen from Fig. 12, DC microgrid cluster has switched its stability during the crossing process. An interesting finding in Fig. 11

and Fig. 12 is that the delay scenario of A1 (3.00, 2.00) is stable, which satisfies $\tau_1 \neq \tau_2$. Although the delay values in the two channels of A1 have already been much bigger than those of A, the cluster can still keep its stability. Hence, it is helpful for the system stability making the time-delay values different.

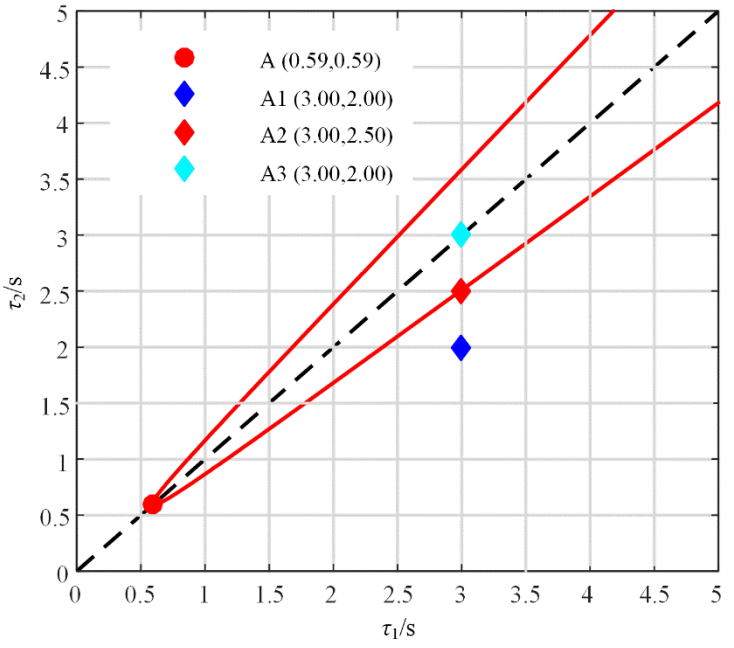

Fig. 11. The kernel boundary in the time-delay space.

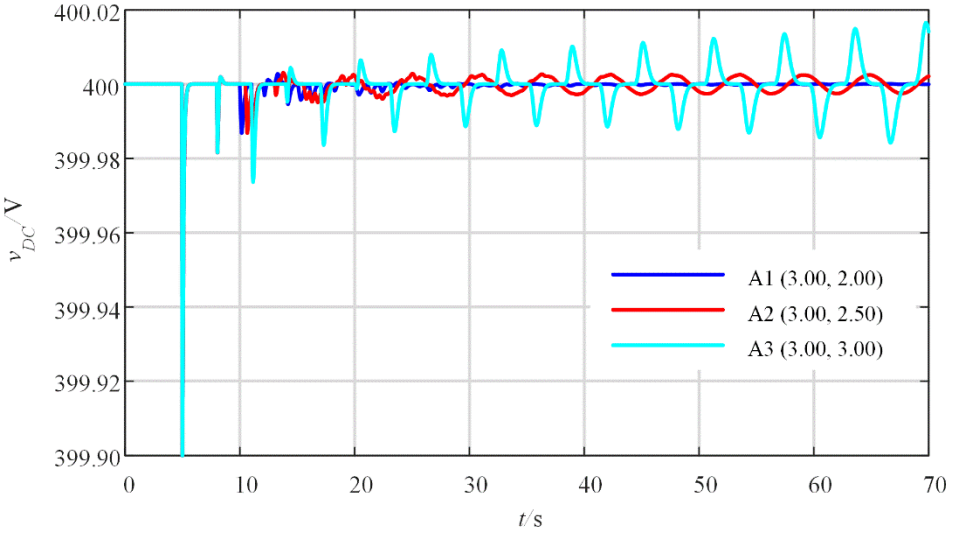

Fig. 12. The bus voltage variations at A1-A3.

In terms of the offspring boundary, the Ors in Fig. 9 are inversely reflected in the three directions likewise. According to the boundaries in Fig. 13, the whole delay space is separated into many regions, which presents a radial pattern. According to the continuity of the linear system [34], the stable region is continuous involving the origin, which is separated from the unstable region by the TDSSB. Even if an infinite number of offspring boundaries will continually reproduce along the three dimensions, there are still many stable areas between TDSSBs.

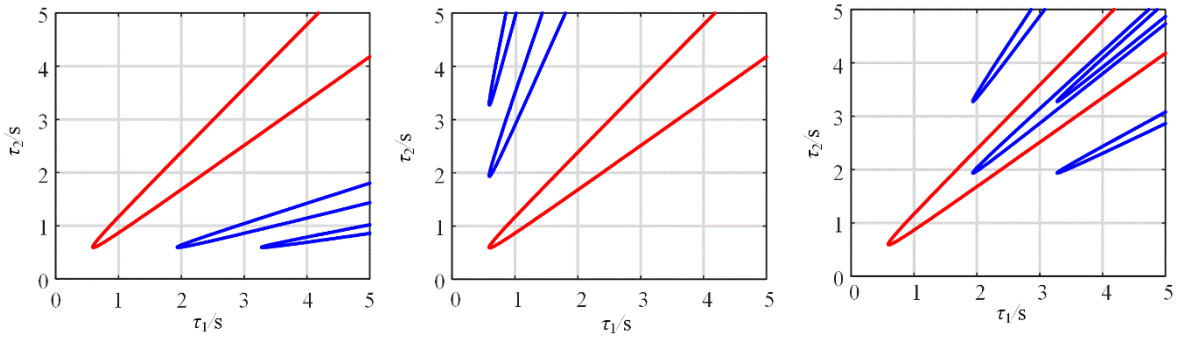

(a) OBs along the τ_1 direction (b) OBs along the τ_2 direction (c) OBs along the (τ_1 , τ_2) direction

Fig. 13. The offspring boundaries along three directions. (Red line: kernel boundary; blue line: offspring boundary)

For the presentation of the TDSSB panorama, all the boundaries in Fig. 13 (a)-(c) are gathered forming Fig. 14.

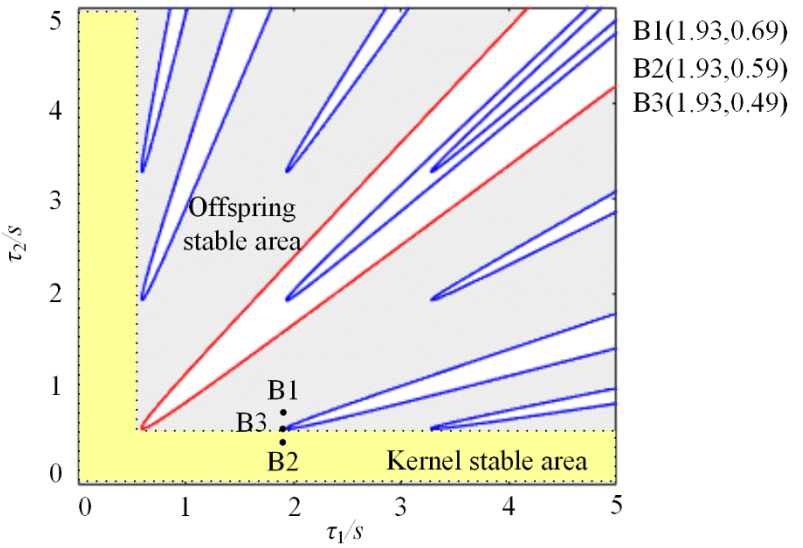

Fig. 14. The TDSSB of the DC microgrid cluster with the distributed control framework.

The benefits of Fig. 13 and Fig.14 to the practical microgrid deployment are in three aspects:

1) Impact visualization. The boundaries in Figure 13 and Figure 14 visualize the time-delay impact for the practical microgrid deployment. According to the distribution of TDSSB in the time-delay space, it can directly judge whether the current time delays can damage the system stability. Supposed the current time delays in Channel 1 and Channel 2 are both 1s, this delay point falls into the unstable area divided by the TDSSB. Hence, the operation in this time-delay state is harmful to the microgrid. In contrast, the microgrid cluster can operate stably with 1s delay in Channel 1 and 1.5s delay in Channel 2, hich locates in the stable area.

2) Stability guidance. Fig. 13 and Fig. 14 are beneficial to protect the practical microgrid deployment from the time-delay instability. According to the time-delay state in different communication channels, these two figures can conveniently provide the guidance strategy. For example, the current delay point is (1, 1) in the unstable area. Instead of maintaining two communication channels simultaneously, the system stability can be effectively enhanced decreasing one time-delay below 0.5s according to Figure 14.

3) Cluster design. On the basis of various requirements from the microgrid cluster, these two figures can be quickly re-plotted guiding the cluster design. Once the TDSSB is very near to the origin, the stability of deployed microgrids would be very sensitive to the time delay. Hence, the design of communication channel should be paid much effort satisfying the time-delay constraints provided by Figure 13 and 14.

The stable region in Fig. 14 can be further classified into two types:

1) Kernel stable area (yellow): This area is surrounded by the KB apex of TDSSB and the dotted line parallel to the delay axes. The apex of KB has the smallest $\|\boldsymbol{\tau}\|_2$ compared to the other points on the TDSSB. The kernel stable area has a regular shape along the axes. The stable points in this area have the same feature that at least one time-delay component is smaller than that of the KB apex.

2) Offspring stable area (cyan): This area is surrounded by all the edges of TDSSB. The edge of each boundary is made up of all the points on the TDSSB. The offspring stable area is an irregular shape encircles the kernel stable area. The stable points in this area have the same feature that they are not in the diagonal direction which indicates all the channel delays are identical.

Kernel stable area and offspring stable area make up the whole stable region for the microgrid cluster. With the TDSSB and the classified stable areas, two strategies can be comfortably proposed to enhance the cluster stability during the cluster design and the real-time operation.

1) Kernel strategy: The DC microgrid can tolerate the time-delay operation by the good maintenance of one communication channel. This strategy can be explained by the time-delay point B1 (1.93, 0.49) in the kernel stable area of Fig. 14. By the preservation of τ_2 in the Channel 2 smaller than 0.59s, the acceptable time-delay value of Channel 1 can be obviously extended along the τ_1 direction. The kernel strategy is helpful to guarantee the cluster stability without spending effort on all the communication channels. Setting a strict condition for one channel, the stability can be significantly improved.

2) Offspring strategy: The DC microgrid can tolerate the time-delay operation by the avoidance of the identical time-delay value. This strategy can be represented by the time-delay point B2 (1.93, 0.69) in the

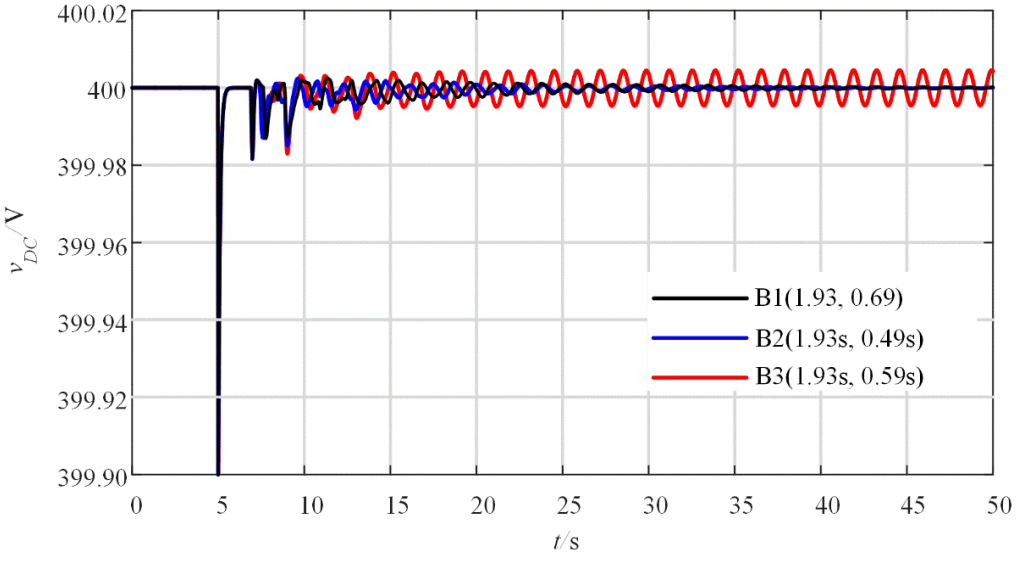

Fig. 15. The stability enhancement by the kernel and the offspring strategies.

stable area of Fig. 14. Although τ_1 in the Channel 1 is much larger than $\tau_2 = 0.69$s, the microgrid cluster can still work stably. The offspring strategy reveals that the non-uniform network is helpful to protect the system stability. The time-delay stability would be weak once all the time-delay components are the same.

These two strategies are demonstrated in Fig. 15. Under the time-delay scenarios at B1 (kernel strategy) and B2 (offspring strategy), the cluster voltage can effectively recover within 5s. Although the kernel and offspring strategies only make small changes to the time delay of Channel 2, the system stability has been significantly enhanced avoiding the oscillations at B3.

On the basis of Fig. 15, the oscillation comparisons of B1-B3 after *t*=10s are displayed in Table 6.

Table 6. Oscillation comparisons of B1-B3.

	B1	B2	B3
Maximum magnitude (10^{-3}V)	5.5	5.6	7.8
Occurrence time (s)	10.9s	12.9s	13.0s

Although the kernel strategy and the offspring strategy are both capable of the stability protection, there are still small differences between this two strategies in Table 6. The magnitude under B1 is the smallest among these three time-delay scenarios. Besides, the corresponding time is also the earliest, i.e., 10.9s. The cluster would experience the maximum oscillation almost 2s later at B2 and B3.

In order to indicate the accuracy of the proposed method, the two stability criteria based on the free-weighting matrix (FWM) [26] and the Jensen inequality (JI) [28] are employed for the following comparison.

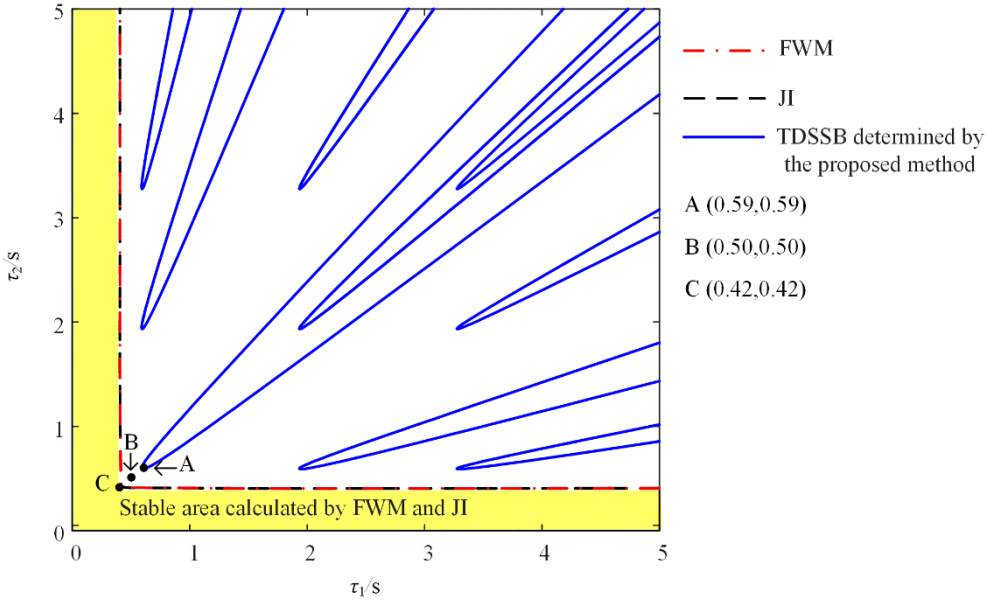

Fig. 16. The TDSSBs calculated by the three methods.

It can be seen from Fig. 16 that the TDSSBs calculated by the stability criteria based on FWM and JI are obviously conservative compared with the determined TDSSB in this paper. The boundaries calculated by FWM and JI are the same, which can only judge the yellow area as the stable area. As

shown in Fig. 16, the large stable area between the dashed line and the solid line will be regarded unstable by FWM and JI. However, the proposed method is able to provide the accurate TDSSB in the blue color. The voltage variations at A (0.59, 0.59), B (0.50, 0.50), and C (0.42, 0.42) are shown in Fig. 17.

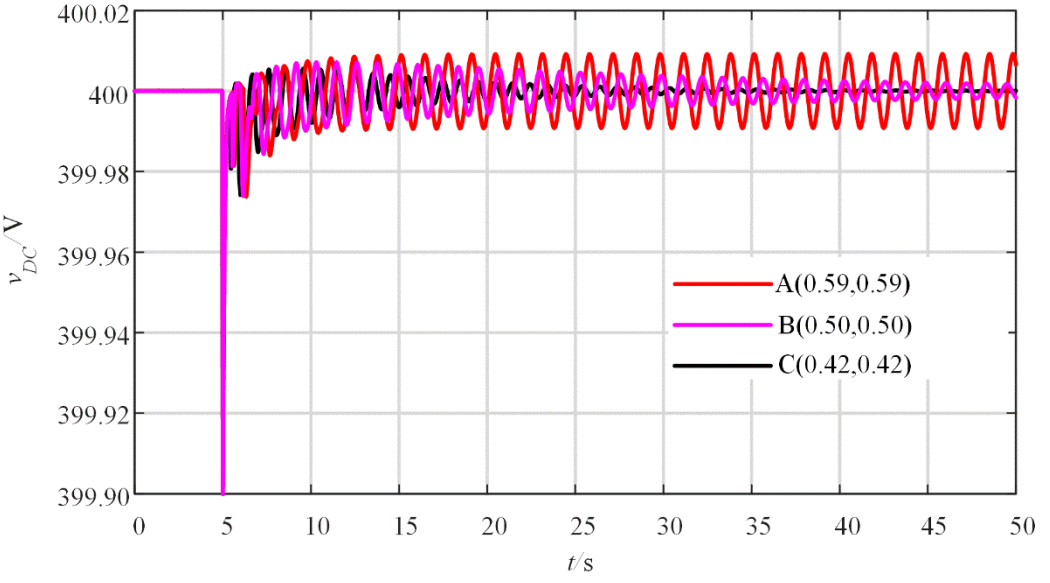

Fig. 17. DC bus voltage variations under different time-delay scenarios of A, B, and C

According to Fig. 17, the DC bus voltage recovers to its nominal value of 400V under the delay scenario of C which is on the calculated TDSSB via the FWM and JI methods. However, the system can still guarantee the stability with the increased delay at B. The equal amplitude oscillation will finally happen at A, which indicates the accurate boundary point with $\tau_1 = 0.59\text{s}$, $\tau_2 = 0.59\text{s}$. To quantitatively analyse the accuracy improvement in this work, the error index is defined as follows

$$\text{Error index} = \frac{\|\boldsymbol{\tau}_A\|_2 - \|\boldsymbol{\tau}_C\|_2}{\|\boldsymbol{\tau}_A\|_2} \times 100\% \tag{42}$$

where $\boldsymbol{\tau}_A$ denotes the point on the TDSSB nearest to the origin calculated by the proposed method, $\boldsymbol{\tau}_C$ denotes the point on the TDSSB nearest to the origin calculated by one method. The error indexes of these three methods are displayed in Table 7.

Table 7. Error indexes of three methods.

	The proposed method	FWM	JI
Error index (%)	0	28.81	28.81

It can be seen from Table 7 that the accuracy of the proposed method is notable. The error indexes of FWM and JI both reached 28.81%. Hence, the TDSSB determination result of the proposed method can provide the accurate time-delay stability information for the DC microgrid cluster.

5. Conclusion

This paper proposes to investigate the explicit time-delay stability for the DC microgrid cluster with the distributed control framework. Through the derived time-delay stability model and the defined time-delay stability switching boundary, the delay issue of the microgrid cluster is accurately examined. In order to determine the complete boundary composed of kernel boundary and offspring boundary, the spectral delay space is deployed to linearize the boundary derivation process. The main findings of this article are presented as follows.

- The time-delay stability switching boundary of the DC microgrid cluster exists, which is made up of the kernel and offspring boundaries;
- The proposed approach is effective to determine the accurate boundary for the DC microgrid cluster;
- The boundary in the time-delay space can be represented by a closed boundary in the spectral delay space;
- The time delay is disclosed as an oscillation source of the DC microgrid cluster;
- The determined boundary divides the stable area in the time-delay space into the kernel and offspring stable areas;
- The time-delay stability of the DC microgrid cluster can be enhanced by setting a strict constraint in one channel or adopting the non-uniform network.

On the basis of this work, we plan to study three major aspects in the future.

- Studying the reason for the existence of the time-delay stability switching boundary;
- Improving the approach efficiency through the reduction of the implementation stages;
- Extending the proposed modeling procedure and systemic analysis to design novel stability enhancement strategies.

Acknowledgments

This work was financially supported by the National High-tech R&D Program of China (2015AA050403) and the National Natural Science Foundation of China (U1766210, 51377117).

References

[1] Report on the government work of the People's Republic of China, 2018; <http://www.mod.gov.cn/top-news/2018-03/05/content_4805962.htm>
[2] Wang CS, Yan JY, Marnay C, Djilali N, Dahlquist E, Wu JZ, Jia HJ. Distributed energy and microgrids (DEM). Applied Energy 2018; **210**: 685-89.
[3] Meng LX, Shafiee Q, Trecate FG, Karimi H, Fulwani D, Lu XN, Guerrero JM. Review on control of DC microgrids and multiple microgrid clusters. IEEE J Emerg Sel Top Power Electron 2017; **5(3)**: 928-48.
[4] Lotfi H, Khodaei A. Hybrid AC/DC microgrid planning. Energy 2017; **118**: 37-46.
[5] Bullich-Massagué E, Díaz-González F, Aragüés-Peñalba M, Girbau-Llistuella F, Olivella-Rosell P, Sumper A. Microgrid clustering architectures. Applied Energy 2018; **212**: 340-61.
[6] Boroojeni K, Amini MH., Nejadpak A, Dragičević T, Iyengar SS, Blaabjerg F. A novel cloud-based platform for implementation of oblivious power routing for clusters of microgrids. IEEE Access 2017; **5**: 607-19.
[7] Amini MH, Boroojeni KG, Dragičević T, Nejadpak A, Iyengar SS, Blaabjerg F. A comprehensive cloud-based real-time simulation framework for oblivious power routing in clusters of dc microgrids. IEEE ICDCM, 2017: 270-73.
[8] Kolluri RR, Mareels I, Alpcan T, Brazil M, Hoog JD, Thomas DA. Power sharing in angle droop controlled microgrids. IEEE Trans Power Sys 2017; **32(6)**: 4743–51.
[9] Moayedi S, Davoudi A. Distributed tertiary control of DC microgrid cluster. IEEE Trans Power Electron 2016; **31(2)**: 1717-

33.
[10] Almada JB, Leão RPS, Sampaio RF, Barroso GC. A centralized and heuristic approach for energy management of an AC microgrid. Renew Sustain Energy Rev 2016, **60**: 1396-404
[11] Bahrami S, Amini MH. A decentralized trading algorithm for an electricity market with generation uncertainty. Applied Energy 2018; **218**: 520-32.
[12] Pasha AM, Zeineldin HH, Al-Sumaiti AS, El-Moursi MS, El Sadaany EF. Conservation voltage reduction for autonomous microgrids based on V–I droop characteristics. IEEE Trans Sustain Energy 2017, **8(3)**: 107
[13] Fani B, Zandi Farshad, Karami-Horestani A. An enhanced decentralized reactive power s
microgrid. Electric Power Energy Syst 2017; **98**: 531–42.
[14] Riverso S, Tucci M, Vasquez JC, Guerrero JM, Ferrari-Trecate G. Stabilizing plug-and-play regulators and secondary coordinated control for AC islanded microgrids with bus-connected topology. Applied Energy 2018; **210**: 914-24.
[15] Bünning F, Sangi R, Müller D. A Modelica library for the agent-based control of building energy systems. Applied Energy 2018; **193**: 52-59.
[16] Xydas E, Marmaras C, Cipcigan LM. A multi-agent based scheduling algorithm for adaptive electric vehicles charging. Applied Energy 2016; **177**: 354-65.
[17] Guo FH, Wen CY, Miao JF, Song YD. Distributed secondary voltage and frequency restoration control of droop-controlled inverter-based microgrids. IEEE Trans Ind Electron 2015; **62(7)**: 4355–64.
[18] Mohammadi FD, Vanashi HK, Feliachi A. State-space modeling, analysis, and distributed secondary frequency control of isolated microgrids. IEEE Trans Energy Convers 2018; **33(1)**: 155–65.
[19] Mo HD, Li YF, Zio E. A system-of-systems framework for the reliability analysis of distributed generation systems accounting for the impact of degraded communication networks. Applied Energy 2016; **183**: 805-22.
[20] Behjati H, Davoudi A, Lewis F. Modular DC–DC converters on graphs: cooperative control. IEEE Trans Power Electron 2014; **29(12)**: 6725–41.
[21] Ren LY, Qin YY, Li Y, Zhang P, Wang B, Luh PB, Song H, Orekan T, Gong T. Enabling resilient distributed power sharing in networked microgrids through software defined networking. Applied Energy 2018; **210**: 1251-65.
[22] Jia HJ, Li XM, Mu YF, Xu C, Jiang YL, Yu XD, Wu JZ, Dong CY. Coordinated control for EV aggregators and power plants in frequency regulation considering time-varying delays. Applied Energy 2018; **210**: 1363-76.
[23] Lai JG, Zhou H, Lu XQ, Yu XH, Hu WS. Droop-based distributed cooperative control for microgrids with time-varying delays. IEEE Trans Smart Grid 2016; **7(4)**: 1775–89.
[24] Ahmadi A, Aldeen M. An LMI approach to the design of robust delay-dependent overlapping load frequency control of uncertain power systems. Int J Electr Power Energy Syst 2016; **81**: 48-63.
[25] Gao QB, Kammer AS, Zalluhoglu U, Olgac N. Critical effects of the polarity change in delayed states within an LTI dynamics with multiple delays. IEEE Trans Automat Control 2015; **60(11)**: 3018-22.
[26] Dong CY, Jia HJ, Jiang T, Bai LQ, Hu QR, Wang L, Jiang YL. Effective method to determine time-delay stability margin and its application to power systems. IET Gener Transm Distrib 2017; **11(7)**: 1661-70.
[27] Medvedeva IV, Zhabko AP. Synthesis of Razumikhin and Lyapunov–Krasovskii approaches to stability analysis of time-delay systems. Automatica 2015; **51**: 372–77.
[28] Zhang CK, He Y, Jiang L, Wu M. Notes on stability of time-delay systems: bounding inequalities and augmented Lyapunov-Krasovskii functionals. IEEE Trans Automat Control 2017; **62(10)**: 5331-36.
[29] Milano F. Small-signal stability analysis of large power systems with inclusion of multiple delays. IEEE Trans Power Sys 2016; **31**: 3257–66.
[30] Gu K, Kharitonov V L, Chen J. Stability of time-delay systems, Springer Birkhauser, 2003.
[31] Gao Q, Olgac N. Bounds of imaginary spectra of LTI systems in the domain of two of the multiple time delays. Automatica 2016; **72**: 235–41.
[32] Feldmann P, Rohrer RA. Proof of the number of independent Kirchhoff equations in an electrical circuit. IEEE Trans Circuit Sys 1991; **38(7)**: 81–84.
[33] Petkov PH, Christov ND, Konstantinov MM. Computational methods for linear control systems. Automatica 1993; **29(2)**: 568–70.
[34] Hale JK, Theory of functional differential equations, Springer-Verlag, New York, 1977.

Response to Reviewer 2: Response 1

Available online at www.sciencedirect.com

ELSEVIER

Applied Energy

Journal homepage: *https://www.journals.elsevier.com/applied-energy/*

Time-delay Stability Switching Boundary Determination for DC Microgrid Clusters with the Distributed Control Framework

Chaoyu Dong[a], Qingbin Gao[b]*, Qian Xiao[a], Xiaodan Yu[a]†, Libor Pekař[c], Hongjie Jia[a]

[a] *School of Electrical and Information Engineering, Tianjin University, Tianjin, 300072, China*
[b] *Department of Mechanical Engineering, The University of Alabama, Tuscaloosa, 35487, USA*
[c] *Faculty of Applied Informatics, Tomas Bata University, Zlin, 76005, Czech Republic*

Abstract

In a DC microgrid cluster, distributed DC microgrids are integrated to manage diverse and distributed energy resources. Without the reliance on a management center, the distributed control framework is capable of the cluster deployment by only adjacent collaborations. However, the communication among microgrids and the formation of dispatch signals inevitably lead to time delays, which might cause the system disorder and multiple-delay couplings. Considering these unstable effects, the lack of time-delay study challenges the cluster stability and burdens the energy application. The key contributions of this paper are the definition and detection of the time-delay stability switching boundary for the DC microgrid cluster with the distributed control framework, which reveals time delays switching the system stability and proves the delay-induced oscillation. Through the established time-delay model and the proposed method based on the cluster treatment of characteristic roots, the explicit time-delay stability switching boundary is detected in the delay space, which forms a determination flow of five stages: 1) system initialization: according to the cluster parameter values, the established time-delay model is initialized; 2) space transformation: applying the space mapping and the rationalization, the Sylvester resultant is constructed in the spectral delay space; 3) spectral boundary sketch: in uniformly divided blocks, spectral boundaries are found from the resultant; 4) crossing root calculation: with the spectral boundaries, crossing roots are calculated solving the characteristic equation; 5) boundary determination: back-mapping the spectral boundaries with the crossing roots, the overall boundary is presented. Comprehensive case studies are performed to study the time-delay stability switching boundary and to validate the proposed approach. The boundary existence and feature demonstrate the time-delay effect. Furthermore, the classified stable areas are revealed as well as the relevant strategies for the stability enhancement.

Keywords: time-delay stability switching boundary, DC microgrid cluster, distributed control, multiple delays

* Corresponding author. Tel.: +1 (475) 200-0351; fax: +1 (562) 985-1503.
E-mail address: qingbin.gao@gmail.com
* Corresponding author. Tel.: +022-27892811; fax: +022-27892811.
E-mail address: yuxd@tju.edu.cn;

The short version of the paper was presented at REM2017, October 18-20, Tianjin, China. This paper is a substantial extension of the short version of the conference paper

Nomenclature

$\boldsymbol{A}_0$	non-delay coefficient	TDSSB	time-delay stability switching boundary
$\boldsymbol{A}_{\tau p}$	time-delay coefficient for τ_p	$\boldsymbol{\tau}$	time-delay vector
$\boldsymbol{A}$	adjacency matrix	$\boldsymbol{\tau}_{KB}$	point on the KB
$\boldsymbol{\alpha}$	integral gain vector	$\boldsymbol{\tau}_{OB}$	point on the OB
α_k	integral gain of k^{th} DC microgrid	$\boldsymbol{u}$	control vector of the secondary layer
CTCR	cluster treatment of characteristic roots	u_k	control signal generated by consensus control
CE	characteristic equation	V^*	nominal DC voltage
$\boldsymbol{D}$	in-degree matrix	v_{Kr}	reflection point on the Kr
FWM	free-weighting matrix	v_{Or}	reflection point on the Or
i	imaginary part of Sylvester resultant	$\boldsymbol{v}_p$	reflection point on the spectral delay space
i_k	output current of k^{th} DC microgrid	v_{droop}	voltage signal generated by droop control
j_p	derivation number for τ_p	v_{DC}	DC bus voltage
JI	Jensen inequality	ω_c	crossing root on the complex plane
KB	kernel boundary	$\boldsymbol{w}_1$	weighting vector for voltage comparison
Kr	kernel reflection	$\boldsymbol{w}_2$	weighting vector for consensus comparison
$\boldsymbol{M}$	Sylvester resultant matrix	w_{1k}	voltage comparison weight of k^{th} DC microgrid
M_k	droop gain of k^{th} DC microgrid	w_{2k}	consensus comparison weight of k^{th} DC microgrid
OB	offspring boundary	x_{1k}	voltage deviation of k^{th} DC microgrid
Or	offspring reflection	x_{2k}	consensus deviation of k^{th} DC microgrid
R_k	line resistance of k^{th} DC microgrid	$\boldsymbol{x}$	deviation vector
r	real part of Sylvester resultant	z_p	tangent substitution variable
τ_p	time delay of the p^{th} channel		

1. Introduction

1.1. Motivation

With the CO_2 emissions and the adverse environmental effects, the traditional fossil fuel is facing a potential crisis of exhaustion and a great curse of pollution. Stimulated by the expectation of beautiful environment and the development of energy conversion [1], dispersive renewable energy sources undertake an unprecedented penetration in both the supply and customer sides. During the transition to a low carbon, green and sustainable society, microgrids provide a promising solution for the integration of distributed energy resources, such as photovoltaics, geothermal and solar heat, wind turbines, microturbines, and various energy storage systems [2]. As a natural and simple solution for utilizing electric power, the development of DC microgrids moves towards a new stage for integrating the renewable energy source and loads. By virtue of DC microgrids, the natural DC outputs from the solar energy can be conveniently supplied to the DC loads like electric vehicles without AC conversions [3]. In the absence of the reactive power and frequency [4], DC microgrids also stay away from many issues such as inrush currents and synchronization. Hence, DC microgrids have emerged as the effective way to upgrade the energy application and evolution.

Despite those merits brought by the DC microgrids, the intermittency of renewable energy and the individual capacity of a single microgrid make the system reliability vulnerable. Once the power output in one microgrid is not able to satisfy the load demand, the load shedding would be inescapable, which may even lead to cascading failures [5]. In order to improve the reliability of a single microgrid, the microgrid

cluster provides an available solution by the connection of distributed units. Through the cloud-based approach [6], multiple DC microgrids can be effectively connected in a meshed network topology. Unaware of the current cluster state and other flows, the proposed oblivious routing algorithm is competent to solve the optimal power flow problem, while managing congestion and mitigating power losses [7]. With the coordination of different energy sources in multiple microgrids, it is not only easy to achieve the power balance [8] but also beneficial to equalize the utilization factors of different devices [9]. In this way, multiple microgrids can help each other and extend their lifespans during various situations.

The control framework for the clustering of multiple microgrids can be classified into centralized, decentralized, and distributed categories. In a centralized control system, there exists at least one control center collecting the data from all the microgrids [10]. After the extraction of operating states from those data, control center generates command signals and sends them back to each microgrid. The centralized framework requires the establishment and maintenance of a high bandwidth network between the control center and every individual microgrid [11]. Because of the high reliance on the communication network and the central controller, the cluster system easily suffers from any failure or accident in these two parts. To improve the system reliability, the decentralized control framework embeds an individual controller in each microgrid [12]. Without the information exchange, every individual controller fulfills its own operation objective. This is a more reliable structure that the control center and the communication network are completely avoided [13]. But this full autonomy is injurious to the system benefit and flexibility due to the lack of global information. As all the microgrids only care about their own operation, the cooperation like the energy sharing is difficult to achieve.

To overcome this problem, the distributed control framework hybridizes the centralized and decentralized structures as a whole. Besides the microgrid [14], the applications of the distributed control framework can be found in other energy systems like the building energy systems [15], electric vehicle systems [16], etc. The distributed control framework can usually be divided into two layers [17]. In the primary control layer, decentralized control strategies such as the droop control are employed to guarantee the independent operation of each microgrid. The secondary control layer then adjusts the individual operation from the cluster aspect. Through the coordination between only neighboring microgrids, the distributed control can achieve the global target as well as the autonomy of every microgrid [18]. For the accomplishment of the reliability and flexibility simultaneously, the distributed control framework provides a viable option for the management of DC microgrid cluster. However, the distributed control framework still requires the communication network to accomplish the global objective. Because the mutual communication and the signal processing take time to finish, the induced time delay becomes an inevitable factor for the distributed control framework.

1.2. Related work

As the open communication network has the high potential for being integrated with future distributed energy systems, the network-induced delays would become obvious due to the limited bandwidth of end-users [19]. It was reported that the dynamics of microgrid currents take much longer time to decay because of the time-delay effect [20]. The authors in [21] suggest that the communication with shorter

time delay is preferable in the microgrid control to protect the system from the possible disorder. Besides those bad effects, the time-delay issue may be more complex and more serious owing to the existence of multiple delays. With two identical delays, the system frequency tends to oscillate [22] without careful configuration. The control algorithms become ineffective taking non-uniform time-varying delays into account [23]. Although those undesirable effects have been mentioned in those studies, accurate time-delay stability analyses have not been carried out yet. Besides, there are few articles devoted to the abovementioned time-delay issue for the DC microgrid cluster in the literature. The lack of the formulated delay model, analysis, and the explicit stability switching information all beset the stability assessment of the microgrid clusters.

For the stability analysis of time delays, the Lyapunov-based method and the eigenvalue-based method are representative. Through the construction of Lyapunov functionals and the deployment of the linear matrix inequality [24], the Lyapunov-based method derives sufficient stability criteria for time-delay systems [25]. The approximate maximum delay without breaking the system stability can then be calculated by various criteria [26]. Although the development of the Lyapunov-based method is speedy, the demerit of conservativeness posts constraints in the stability analysis [27]. The lack of a unified and systematic approach predisposes most Lyapunov functionals to extreme difficulties for construction. Moreover, various inequalities during the derivation process aggravate the inaccuracy by the introduction of scaling errors [28]. Therefore, those conservative results are not accurate to provide the factual time-delay boundary for DC microgrid clusters.

By contrast, eigenvalue-based methods determine the time-delay margin by computing purely imaginary roots of characteristic equations, which can deliver the more exact results. In [29], Padé approximants were used to evaluate the transcendental terms in the characteristic equation. The crossing root was then calculated with the corresponding time delays. Through the construction of the Schur-Cohn-Fujiwara matrix and the eigenvalues of the Hamiltonian matrix, [30] calculated the delay margin for the linear delay systems. But both of them only reckoned the minimum margin, which is ineffective to determine the complete information of all stability switching boundaries. To overcome this problem, the cluster treatment of characteristic roots (CTCR) [31] were proposed to establish the relationship between the time-delay space and the spectral delay space. Employing the root-clustering feature, the concepts of “kernel” and “offspring” are also introduced, which imparts the complete portrait of the possible imaginary root crossings of time-delay systems.

The difference comparisons of those methods can be presented from three aspects:

1) Objective. CTCR technique aims to find out all the time delays switching the system stability, which can provide complete stability switching information caused by the time delays. However, other methods like [29] only calculate the minimum delay value that a time-delay system can endure. Without complete stability information related to time-delay, very strict time-delay constraints might be introduced during the microgrid cooperation, which would lead to the unnecessary cost and control;

2) Application range. For the employment of existing methods in [30], the time-delay values in different communication channels should be assumed the same, .i.e., the suitability of single-delay analyses. However, CTCR is carried out in the time-delay space, which is capable of single-delay and multiple-delay analyses simultaneously;

3) Accuracy. As the constructed results in CTCR is the necessary and sufficient condition for the time-delay stability judgment, critical time delays can be determined accurately. But Lyapunov-based methods like [26] can only provide sufficient stability criteria for time-delay analyses. The calculation results are conservative.

Notwithstanding those merits of the CTCR, whether it is suitable for the time-delay analysis of DC microgrid cluster and how to implement this technique have not been investigated so far.

1.3. Contribution

This paper presents a systemic analysis approach including the time-delay model, analysis method, and stability switching investigation for the DC microgrid cluster with the distributed control framework. With the droop control in the primary layer and the consensus control in the secondary layer, a distributed control framework is utilized to manage the power dispatch and the DC voltage of the cluster. Based on this demonstrated DC microgrid cluster, a global analysis model is then built to incorporate the time delays in the coordination network. In order to figure out all the stability switching scenario, the time-delay stability switching boundary (TDSSB) is defined mathematically for the DC microgrid cluster, which reveals the explicit transition from stability to instability as well as a theoretical proof for the oscillation phenomenon induced by the time delays. Considering the coupling of the variable crossing roots and the delay components in the TDSSB definition, the CTCR technique is employed to convert the issue in the time-delay space to the spectral delay space, based on which we design a streamline of five stages for the TDSSB determination. With the system initialization and the space transformation as the first two stages, the rationalized Sylvester resultant can be constructed. After that, the spectral boundary sketch and the crossing root calculation are implemented to search the critical points in the spectral delay space and the relevant oscillating frequencies. According to the relationship between these two spaces, the objective of TDSSB determination can be achieved in the last stage, which assembles the overall time-delay points switching the stability of the DC microgrid cluster.

Four major contributions of this paper are summarized as below.

1) TDSSB is defined mathematically for the DC microgrid cluster with the distributed control framework and proved as an oscillation source;

2) A time-delay stability analysis model for the DC microgrid cluster with the distributed control framework is derived, which facilitates model-based investigations for the global stability of the cluster;

3) Based on the time-delay model, a systematic method is proposed to determine the TDSSB of the DC microgrid cluster by utilizing the CTCR. By the designed implementation flow of five stages, the TDSSB panorama can be presented effectively;

4) From the single-delay scenario to the multiple-delay one, the accurate TDSSB is determined and validated for the DC microgrid cluster with the distributed control framework. With the help of the explicit TDSSB, stable areas can be divided advancing stability tactics for the microgrid cluster.

1.4. Organization

The rest of this paper is organized as follows. Section 2 specifies the derivation and analyses of the time-delay model for the DC microgrid cluster with the distributed control framework. In Section 3, a

CTCR-based method is proposed to determine the accurate TDSSB as well as a designed streamline of five stages. Case studies are presented in Section 4 where three different scenarios are carefully investigated. Based on the determined TDSSB, two strategies are also raised to improve the time-delay stability. Besides, the accuracy of the proposed method is indicated comparing with existing methods. Finally, we present the summary and conclusion of this work in Section 5.

2. Time-delay model for the DC microgrid cluster with the distributed control framework

In this study, the DC microgrid cluster with the distributed control framework is depicted in Fig. 1. With the DC microgrid cluster of Fig. 1, the distributed DC microgrid 1,…, DC microgrid *k*,…, DC microgrid *n* are aggregated to a relatively larger system. During the operation of this cluster, the energies can be reasonably dispatched among multiple microgrids. It is beneficial not only for the proper employment of diverse energy sources from the solar panels and batteries, but also for the satisfaction of various requirements from time-variant loads.

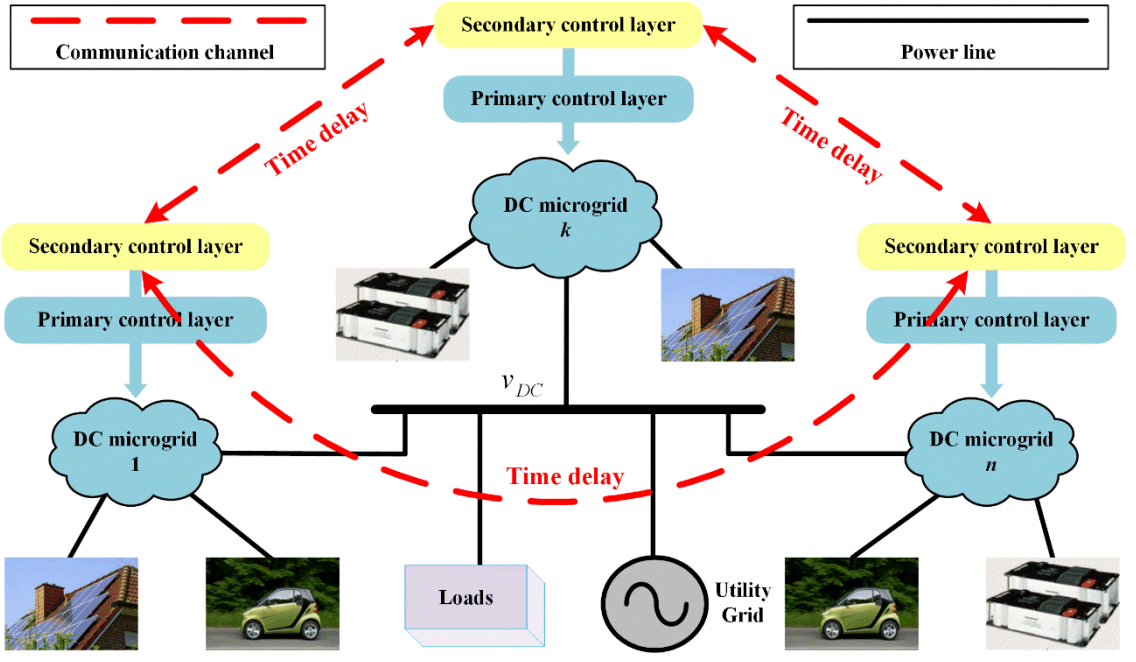

Fig. 1. The DC microgrid cluster with the distributed control framework.

As shown in Fig. 1, the distributed control framework is made up of two control layers to manage the DC microgrid cluster. In the primary control layer, the control objective is designed to guarantee the fundamental operation of every microgrid. Measuring only the local information like the output currents and the terminal voltages, all the microgrids are capable of independent operations, which benefits the reliability of the whole system. Meanwhile, the secondary control layer utilizes the sparse network to adjust the control signals. Through only the neighboring interactions, the global control objective like the preservation of the common DC voltage can be achieved without a central controller. However, the distance between microgrids is not always close enough, which would make the time delays in the communication channels (represented by red dashed lines in Fig. 1) unavoidable. Indeed, there may exist multiple time delays in different exchange channels. Once any coupling happens among those multiple

delays, unrevealed risks might occur and even affect the stability of the whole cluster. For the stability investigation via a model-based approach, the distributed control framework with the droop control and the consensus control is utilized as an instance.

2.1. DC microgrid cluster with the primary droop control

In order to control the DC microgrid cluster in a decentralized approach, the droop control is widely employed for the power sharing [3]. According to the output current i_k and the droop gains M_k, the voltage reference is generated for each microgrid

$$v_{droop}(t) = V^* - M_k i_k(t) \tag{1}$$

where V^* is the nominal bus voltage of the common DC bus.

Considering the line resistance between the microgrid and the common bus, the DC bus voltage v_{DC} is obtained as

$$v_{DC}(t) = v_{droop}(t) - R_k i_k(t) \tag{2}$$

where R_k, k=1,2,…,n, is the line resistance, respectively. From (1)-(2), the real-time v_{DC} is expressed as

$$v_{DC}(t) = V^* - (M_k + R_k) i_k(t) \tag{3}$$

As the DC microgrids are connected parallel to the common DC bus shown in Fig. 2, (3) holds for all the microgrids, which implies $(M_k + R_k) i_k(t) = (M_l + R_l) i_l(t), \forall k, l$. Thus, the output currents of all the DC microgrids can be pre-designed proportionally by setting the droop gains much larger than the line resistances. However, this control strategy will cause the inevitable voltage deviation between v_{DC} and V^* in (3). As the DC bus is the main concern for the microgrid cluster, the bus voltage must be compensated by proper strategies.

2.2. Time-delay in the secondary consensus control

Without the global information exchange, the consensus control strategy provides a powerful strategy only employing the adjacent cooperation. In Fig. 2, the consensus control in [17] is demonstrated here. Two kinds of deviation information are collected to generate the control signal $u_k(t)$ for the voltage recovery. With the measured bus voltage, the voltage deviation $x_{1k}(t)$ is obtained in the k^{th} DC microgrid

$$x_{1k}(t) = V^* - v_{DC}(t) \tag{4}$$

Besides the voltage deviation, neighboring control signals are compared to keep the power ratio determined by the droop control, which forms the consensus deviation

$$x_{2k}(t) = \sum_{l \in N_k} [u_l(t - \tau_{lk}) - u_k(t)] \tag{5}$$

where N_k is the neighborhood set of the k^{th} microgrid, τ_{kl} is the time delay during the message exchange between k^{th} DC microgrid and l^{th} DC microgrid. Denoting $\boldsymbol{u}(t) = [u_1(t), \ldots, u_k(t), \ldots, u_n(t)]^T$, the vector of consensus errors $\boldsymbol{x}_2(t) = [\boldsymbol{x}_{21}(t), \ldots, \boldsymbol{x}_{2k}(t), \ldots, \boldsymbol{x}_{2n}(t)]^T$ can be obtained from (5)

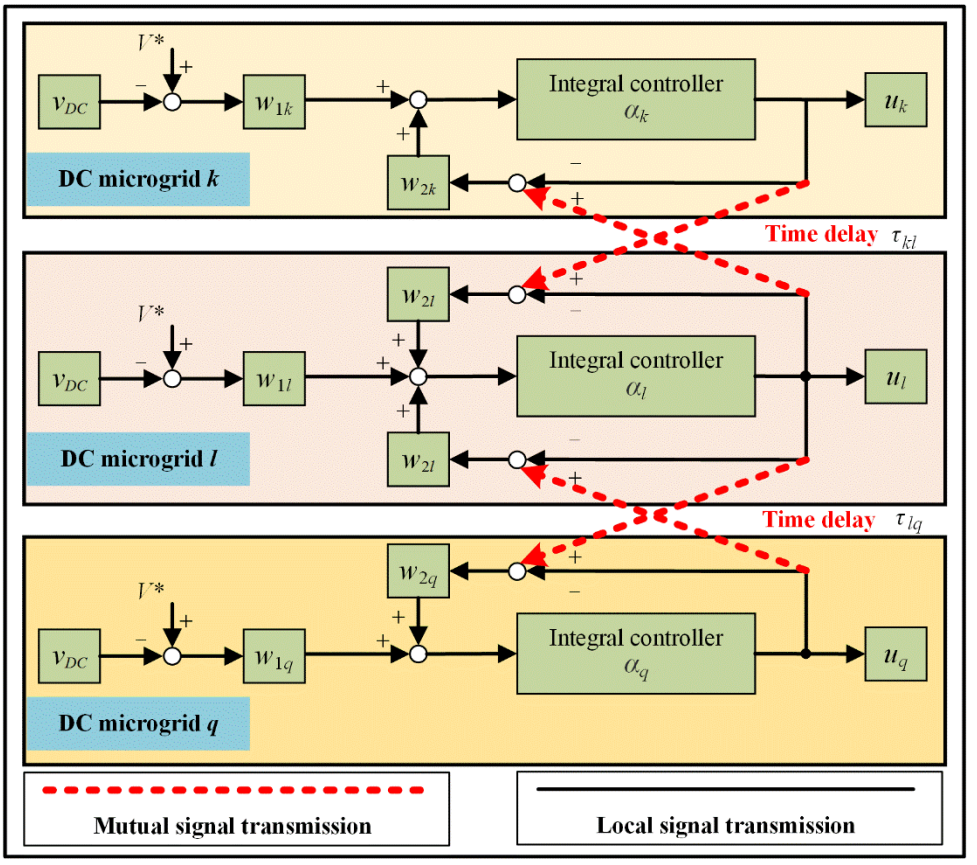

Fig. 2. The secondary consensus control for the DC microgrid cluster.

(The secondary control signals u_k/ u_l/ u_q are formed through the embedded integral controllers α_k/ α_l/ α_q based on the weighted voltage deviations via w_{1k}/ w_{1l}/ w_{1q} and the weighted consensus deviations via w_{2k}/ w_{2l}/ w_{2q}. Time delays τ_{kl} and τ_{lq} occur during the neighboring interactions among k^{th}/l^{th}/q^{th} DC microgrids.)

$$\boldsymbol{x}_2(t) = \sum_{p=1}^{m} \boldsymbol{A}_p \boldsymbol{u}(t-\tau_p) - \boldsymbol{D}\boldsymbol{u}(t) \tag{6}$$

where $\sum \boldsymbol{A}_p = \boldsymbol{A}$, p=1,2,…,m, is the index of each channel, $\boldsymbol{A} = [a_{kl}] \in \mathbf{R}^{n\times n}$ is the adjacency matrix, the element $a_{kl} = a_{lk} = 1$ if $l \in N_k$; otherwise, $a_{kl} = a_{lk} = 0$; $\boldsymbol{A}_p = [a_{pkl}] \in \mathbf{R}^{n\times n}$, $a_{pkl} = a_{plk} = 1$, $\tau_p = \tau_{kl} = \tau_{lk}$, if (k,l) forms the channel p; otherwise, $a_{pkl} = a_{plk} = 0$; $\boldsymbol{D} \in \mathbf{R}^{n\times n}$ is the diagonal in-degree matrix with $\boldsymbol{D}_{kk} = \sum_{l=1}^{n} a_{kl}$. If all the delay values are 0, v_{DC} can recovered to V^* with pre-designed droop gains when (4)-(5) converge to 0. But the communication and the signal process always induce time delays. Hence, the derivation of a time-delay stability analysis model for the DC microgrid cluster becomes necessary.

2.3. Time-delay model for the global stability analysis

In order to achieve the voltage restoration without affecting the power allocation, the consensus control output $\boldsymbol{u}(t)$ is added for the voltage reference adjustment in the droop control. According to (4) and the adjusted reference in (3), the real-time $\boldsymbol{x}_1(t) = [\boldsymbol{x}_{11}(t),\ldots,\boldsymbol{x}_{1k}(t),\ldots,\boldsymbol{x}_{1n}(t)]^T$ becomes

$$\boldsymbol{x}_1(t) = \boldsymbol{D}_{RM}\boldsymbol{i}(t) - \boldsymbol{u}(t) \tag{7}$$

where $\boldsymbol{D}_{RM} = diag\{R_k + M_k\}$, $\boldsymbol{i}(t) = [i_1(t),\ldots,i_k(t),\ldots,i_n(t)]^T$.

For the further derivation of the system model, the common resistance load is taken as an example. Assuming R to be the equivalent resistance of all loads, the relevant load current $i_L(t)$ can be obtained

$$i_L(t) = v_{DC}(t) / R \tag{8}$$

According to the Kirchhoff's Circuit Law [32], $i_L(t)$ equals to the sum of $i_k(t)$, k=1,2,…, n

$$i_L(t) = \sum_{k=1}^{n} i_k(t) \tag{9}$$

Combining (8) and (9), the DC bus voltage is expressed by the load resistance R and the branch current of each microgrid

$$v_{DC}(t) = R\sum_{k=1}^{n} i_k(t) \tag{10}$$

The relationship between the microgrid currents and control signals is then derived from (10) and (3)

$$\boldsymbol{i}(t) = \boldsymbol{Z}^{-1}V^*\boldsymbol{I}_{n\times 1} + \boldsymbol{Z}^{-1}\boldsymbol{u}(t) \tag{11}$$

where $\boldsymbol{Z} = \boldsymbol{D}_{RM} + R\boldsymbol{I}_{n\times n}$, $\boldsymbol{D}_{RM} = diag\{R_k + M_k\}$, $\boldsymbol{I}_{n\times n}$ is the $n\times n$ matrix with all elements being 1, $\boldsymbol{I}_{n\times 1}$ is the $n\times 1$ vector with all elements are 1.

Based on (11) and (7), $\boldsymbol{x}_1(t)$ can be reflected by $\boldsymbol{u}(t)$

$$\boldsymbol{x}_1(t) = \boldsymbol{D}_{RM}\boldsymbol{Z}^{-1}V^* \cdot \boldsymbol{I}_{n\times 1} - R\boldsymbol{I}_{n\times n}\boldsymbol{Z}^{-1}\boldsymbol{u}(t) \tag{12}$$

Denoting $\boldsymbol{w}_1 = diag\{w_{11},\cdots,w_{k1},\cdots,w_{n1}\}$ and $\boldsymbol{w}_2 = diag\{w_{12},\cdots,w_{k2},\cdots,w_{n2}\}$ as the weighting vectors for $\boldsymbol{x}_1(t)$ and $\boldsymbol{x}_2(t)$ respectively, the summation of deviation $\boldsymbol{x}(t)$ can be written as

$$\boldsymbol{x}(t) = \boldsymbol{w}_1\boldsymbol{x}_1(t) + \boldsymbol{w}_2\boldsymbol{x}_2(t) \tag{13}$$

Substituting (12) and (6) into (13) yields

$$\boldsymbol{x}(t) = \boldsymbol{w}_1[\boldsymbol{D}_{RM}\boldsymbol{Z}^{-1}V^* \cdot \boldsymbol{I}_{n\times 1} - R\boldsymbol{I}_{n\times n}\boldsymbol{Z}^{-1}\boldsymbol{u}(t)] + \boldsymbol{w}_2\sum_{p=1}^{m}\boldsymbol{A}_p\boldsymbol{u}(t-\tau_p) - \boldsymbol{w}_2\boldsymbol{D}\boldsymbol{u}(t) \tag{14}$$

The dynamics of the cluster can then be obtained by the derivative of (13) with respect to t

$$\frac{d\boldsymbol{x}(t)}{dt} = -(\boldsymbol{w}_1R\boldsymbol{I}_{n\times n}\boldsymbol{Z}^{-1} + \boldsymbol{w}_2\boldsymbol{D})\frac{d\boldsymbol{u}(t)}{dt} + \boldsymbol{w}_2\sum_{p=1}^{m}\boldsymbol{A}_p\frac{d\boldsymbol{u}(t-\tau_p)}{dt} \tag{15}$$

As the secondary consensus control utilizes the integral component to eliminate the total error in Fig. 2, the derivatives of the control vectors $\boldsymbol{u}(t-\tau_p)$, $\boldsymbol{u}(t)$ are $\boldsymbol{\alpha}\boldsymbol{x}(t-\tau_p)$ and $\boldsymbol{\alpha}\boldsymbol{x}(t)$ respectively, where $\boldsymbol{\alpha} = diag\{\alpha_1,\cdots,\alpha_k,\cdots,\alpha_n\}$, α_k, k=1,2,…,n, are the integral gains. Therefore, (15) can be rewritten as

$$\frac{d\boldsymbol{x}(t)}{dt} = \boldsymbol{A}_0\boldsymbol{x}(t) + \sum_{p=1}^{m}\boldsymbol{A}_{\tau p}\boldsymbol{x}(t-\tau_p) \tag{16}$$

where $\boldsymbol{A}_0 = -(\boldsymbol{w}_1R\boldsymbol{I}_{n\times n}\boldsymbol{Z}^{-1} + \boldsymbol{w}_2\boldsymbol{D})\boldsymbol{\alpha}$, $\boldsymbol{A}_{\tau p} = \boldsymbol{w}_2\boldsymbol{A}_p\boldsymbol{\alpha}$. Different from a small signal stability model close to a certain operation point, (16) provides a time-delay model for the global stability analysis of DC microgrid cluster without the needed linearization procedure.

3. Time-delay stability switching boundary (TDSSB) determination

As the stable operation is the main concern for the cluster, it is important to keep the whole system far away from any unstable state caused by the time-delay part in the model (16). In this section, the TDSSB is defined in the time-delay space revealing all the stability switching delays. A TDSSB determination method and the corresponding implementation flow are then proposed for the DC microgrid cluster.

3.1. TDSSB definition

The characteristic equation of the DC microgrid cluster (16) is

$$\mathrm{CE}(s,\boldsymbol{\tau}) = \det\left(s\boldsymbol{I} - \boldsymbol{A}_0 - \sum_{p=1}^{m} \boldsymbol{A}_{\tau p} e^{-\tau_p s}\right) \tag{17}$$

where s is the Laplace operator, $\boldsymbol{\tau} = [\tau_1,...,\tau_p,...,\tau_m]^T \in \mathbf{R}^m$ indicates a point in the time-delay space composed of m time-delay components.

With all the eigenvalues of the matrix $\boldsymbol{A}_0 + \sum_{p=1}^{m} \boldsymbol{A}_{\tau p}$ designed on the left side of the complex plane, the system stability can be guaranteed in the ideal zero-delay scenario, i.e., $\boldsymbol{\tau} = \mathbf{0}$. But the fact that $\boldsymbol{\tau} \neq \mathbf{0}$ during the practical operation makes the transcendental terms in (17) non-constants, which becomes uncertain risks for the cluster stability.

In order to sort out all the time-delay points switching the DC microgrid cluster stability, the time-delay stability switching boundary (TDSSB) is defined in the time-delay space

$$\mathrm{TDSSB} = \{\boldsymbol{\tau} \mid \det\left(i\omega_c \boldsymbol{I} - \boldsymbol{A}_0 - \sum_{p=1}^{m} \boldsymbol{A}_{\tau p} e^{-i\tau_p \omega_c}\right) = 0, \boldsymbol{\tau} \in \mathbf{R}^{n+}, \omega_c \in \mathrm{R}^+\} \tag{18}$$

where $i\omega_c$ is the crossing root in the complex plane. In the definition above, any point on the TDSSB is associated with at least one purely imaginary root of the system characteristic equation. It can be seen from (18) that two constraints of $\boldsymbol{\tau} \in \mathbf{R}^{n+}$ and $\omega_c \in \mathrm{R}^+$ have been posted for the TDSSB. During the operation of the DC microgrid cluster, each component of the time-delay points is positive, which makes $\boldsymbol{\tau} \in \mathbf{R}^{n+}$. In terms of the other constraint $\omega_c \in \mathrm{R}^+$, a theorem is given as follows.

Theorem 1: The time delays τ_p, p=1,2,…,m, do not induce the crossing root through the origin for the DC microgrid cluster model (16).

Proof: This is a proof by contradiction. If the time delays τ_p, p=1,2,…,m, induce the crossing root through the origin, there exists at least one $\boldsymbol{\tau}$ associated with $\omega_c = 0$. In other words, λ=0 would become an eigenvalue of $\boldsymbol{A}_0 + \sum_{p} \boldsymbol{A}_{\tau p}$. But all the eigenvalues $\boldsymbol{A}_0 + \sum_{p} \boldsymbol{A}_{\tau p}$ have been designed negative for $\boldsymbol{\tau} = \mathbf{0}$ in the time-delay space. Here comes the contradiction. Q.E.D.

On the basis of this theorem, only $\omega_c \neq 0$ needs to be considered for the TDSSB, which means that time delays are potential sources for oscillations. According to the conjugation of imaginary roots, the range of ω_c is further narrowed to R^{n+}. Therefore, the defined TDSSB includes all the essential time-

delay points despite these conditions. As the exponential term $e^{-i\tau_p\omega_c}$ has the period of 2π concerning the product of τ_p and ω_c, the defined TDSSB can be categorized into two sub-boundaries:

Kernel Boundary (KB): The boundary that consists of all the points $\boldsymbol{\tau} \in \mathbf{R}^{n+}$ corresponding to $i\omega_c$ occurrence and satisfies the constraint $0 < \tau_p\omega_c < 2\pi$, p=1,2,…, m. This constraint entails that the points on the KB display the smallest delay compositions.

Offspring Boundary (OB): The boundary is derived from the KB by the following point-wise transformation

$$(\tau_1 \pm 2\pi j_1 / \omega_c, ..., \tau_p \pm 2\pi j_p / \omega_c, ..., \tau_m \pm 2\pi j_m / \omega_c) \tag{19}$$

where j_p=1,2,…,∞, are not zeroes simultaneously. It can be seen from (19) that any point on the KB results in ∞^n (n-dimensional infinity) OB over the identical crossing root $i\omega_c$.

Instead of determining infinite number of boundaries, this classification reveals that keeping track of the KB is more effective and efficient. However, the coupling of two variables, i.e., $\boldsymbol{\tau}$ and $i\omega_c$ in the characteristic equation (18), forms the main challenge for the determination of TDSSB. Moreover, the nonlinear transformation (19) has the variable ω_c as the denominator, which hampers the analysis.

3.2. Spectral delay space mapping

In order to settle those two problems, the spectral delay space is introduced by the technique of cluster treatment of characteristic roots (CTCR) [31]. The conditional mapping rule is given as follows:

If a delay set $\boldsymbol{\tau} \in \mathbf{R}^{n+}$ induces the imaginary root $i\omega_c$, then $\boldsymbol{\nu} = \boldsymbol{\tau}\omega_c$ forms a point in the spectral delay space. On the contrary, the left points in the time-delay space are not presented.

According to this mapping rule, the representation of KB in the spectral delay space is denoted as the kernel reflection (Kr)

$$\mathrm{Kr} = \{\boldsymbol{\nu}_{Kr} \mid \boldsymbol{\tau}_{KB} \in \mathrm{KB}, 0 < \boldsymbol{\nu}_{Kr}^T \boldsymbol{e}_p < 2\pi, p = 1,2,...,m\} \tag{20}$$

where $\boldsymbol{e}_p = [0,\ldots,1,\ldots,0]^T$ is a unit vector, $\boldsymbol{e}_p(p,1) = 1$. Similarly, the OB projection is called the offspring reflection (Or)

$$\mathrm{Or} = \{\boldsymbol{\nu}_{Or} \mid \boldsymbol{\tau}_{OB} \in \mathrm{OB}, \boldsymbol{\nu}_{Or}^T \boldsymbol{e}_p > 2\pi, p = 1,2,...,m\} \tag{21}$$

On the basis of the mapping rule above, the characteristic equation of the DC microgrid with the distributed control framework can then be rewritten in the spectral delay space as

$$\mathrm{CE}(\omega_c, \boldsymbol{\nu}) = \det\left(i\omega_c \boldsymbol{I} - \boldsymbol{A}_0 - \sum_{p=1}^{m} \boldsymbol{A}_{\tau p} e^{-i\nu_p}\right) \tag{22}$$

Remark:

According to (20)-(22), there are three merits of the spectral delay space mapping:

1) Numerical simplification: Without searching in the space of the infinite length on each edge, only Kr needs to be determined in the limited space;

2) Linearized Transformation: The transition from the Kr to the Or is easily fulfilled by stacking the copies of the Kr, which avoids the undesirable distortion due to the point-wise nonlinear transformation;

3) Boundary isolation: The whole space can be evenly divided into small blocks with the lengths of 2π, which isolates all the boundaries from each other.

3.3. TDSSB determination

As the existence of exponential terms still causes the troubles for solving (22), they are replaced with the Euler's formula

$$e^{-iv_p} = \cos(v_p) - i\sin(v_p),\ p = 1,2,...,m \tag{23}$$

Denoting $z_p = \tan(v_p / 2)$, (23) is then rewritten by the half-angle tangent

$$e^{-iv_p} = \frac{1-z_p^2}{1+z_p^2} - i\frac{2z_p}{1+z_p^2} \tag{24}$$

By substituting (24) into (23), the characteristic equation is rationalized as

$$\mathrm{CE}(\omega_c, z_1, \ldots, z_m) = \det\left[i\omega_c \boldsymbol{I} - \boldsymbol{A}_0 - \sum_{p=1}^{m} \boldsymbol{A}_{\tau p}\left(\frac{1-z_p^2}{1+z_p^2} - i\frac{2z_p}{1+z_p^2}\right)\right] \tag{25}$$

For different crossing roots, any solution needs to make both real and imaginary parts of (25) vanish

$$\mathrm{Re}[\mathrm{CE}(\omega_c, z_1, \ldots, z_m)] = 0 \tag{26}$$

$$\mathrm{Im}[\mathrm{CE}(\omega_c, z_1, \ldots, z_m)] = 0 \tag{27}$$

To guarantee these two equations established under any crossing root $i\omega_c$, the Sylvester matrix [33] is formed to be singular

$$|\boldsymbol{M}| = \begin{vmatrix} r_h(z_1,...,z_m) & \cdots & r_0(z_1,...,z_m) & 0 & \cdots & 0 & 0 \\ 0 & r_h(z_1,...,z_m) & \cdots & r_0(z_1,...,z_m) & 0 & \cdots & 0 \\ \vdots & \ddots & \ddots & \ddots & \ddots & \ddots & \vdots \\ 0 & \cdots & 0 & 0 & r_h(z_1,...,z_m) & \cdots & r_0(z_1,...,z_m) \\ i_l(z_1,...,z_m) & \cdots & i_0(z_1,...,z_m) & 0 & \cdots & 0 & 0 \\ 0 & i_l(z_1,...,z_m) & \cdots & i_0(z_1,...,z_m) & 0 & \cdots & 0 \\ \vdots & \ddots & \ddots & \ddots & \ddots & \ddots & \vdots \\ 0 & \cdots & 0 & 0 & i_l(z_1,...,z_m) & \cdots & i_0(z_1,...,z_m) \end{vmatrix} = 0 \tag{28}$$

where $r_h(z_1,\ldots,z_m),...,r_0(z_1,\ldots,z_m)$ are the real-part coefficients, h is the degree of (26); $i_l(z_1,\ldots,z_m),...,i_0(z_1,\ldots,z_m)$ are the imaginary-part coefficients, l is the degree of (27).

Depending on the relationship between the kernel reflection and the offspring ones, the derivation rule from the Kr to the Or is as follows

$$\mathrm{Or} = \{\boldsymbol{v}_{Or} \mid \boldsymbol{v}_{Kr} \in \mathrm{Kr}, \boldsymbol{v}_{Or} = \boldsymbol{v}_{Kr} + 2\pi j_p \boldsymbol{e}_p\} \tag{29}$$

where j_p, $p = 1,2,...,m$ are the derivation number. Their values cannot be 0 at the same time.

While an infinite number of Ors are generated from the derivation rule (29), the corresponding crossing roots remained the same compared to those regarding the Kr. With the knowledge of all the crucial $\tilde{z}_p$ from (28), ω_c becomes the only variable, which results in the equation below

$$\det\left[i\omega_c \boldsymbol{I} - \boldsymbol{A}_0 - \sum_{p=1}^{m} \boldsymbol{A}_{\tau p}\left(\frac{1-\tilde{z}_p^2}{1+\tilde{z}_p^2} - i\frac{2\tilde{z}_p}{1+\tilde{z}_p^2}\right)\right] = 0 \tag{30}$$

The kernel boundary and the offspring boundary of TDSSB are then obtained by the inverse transformations below

$$\mathrm{KB} = \{\boldsymbol{\tau}_{KB} \mid \boldsymbol{\nu}_{Kr} \in \mathrm{Kr}, \boldsymbol{\tau}_{KB} = \boldsymbol{\nu}_{Kr} / \omega_c\} \tag{31}$$

$$\mathrm{OB} = \{\boldsymbol{\tau}_{OB} \mid \boldsymbol{\nu}_{Or} \in \mathrm{Or}, \boldsymbol{\tau}_{OB} = \boldsymbol{\nu}_{Or} / \omega_c\} \tag{32}$$

3.4. Implementation flow for the TDSSB determination

In light of Section 3.1-3.3, an implementation flow of five stages is designed to determinate the TDSSB for the DC microgrid cluster.

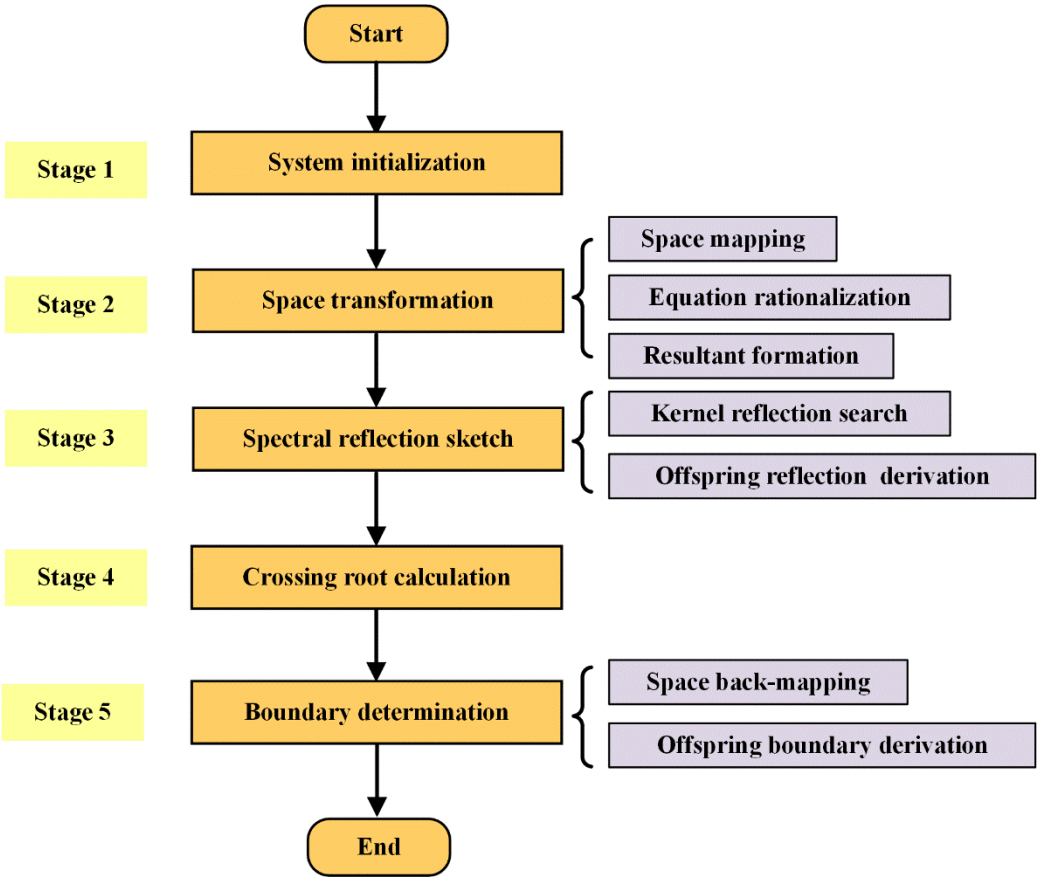

Fig. 3. Implementation flow for the TDSSB determination of the DC microgrid cluster.

Each stage in the flowchart in Fig. 3 is detailed as follows.

Stage 1: System initialization.

With the parameters of the DC microgrid cluster, the coefficients in the time-delay model (16) and the derivation number j_p are initialized.

Stage 2: Space transformation.

a) Space mapping. Introducing $\boldsymbol{\nu} = \boldsymbol{\tau}\omega_c$, the characteristic equation (22) is obtained in the spectral delay space mapped from the time-delay space;

b) Equation rationalization. To eliminate the exponential terms, the half-angle tangent substitution is employed to form (25);

c) Resultant formation. Extracting the real-part coefficients and imaginary-part coefficients from the equation rationalization, the Sylvester resultant in (28) is constructed;

Stage 3: Spectral boundary sketch.

a) Kernel reflection search. Within 2π length on each side, critical points are solved rendering $\boldsymbol{M}$=0;

b) Offspring reflection derivation. On the basis of the derivation rule in (29) and j_p, Ors are derived quantitatively duplicating the Kr;

Stage 4: Crossing root calculation.

All the crossing roots are calculated solving (30) as well as the oscillating frequencies dividing by 2π;

Stage 5: Boundary determination.

a) Space back-mapping. The KB of the DC microgrid cluster is obtained in the time-delay space with the inverse transformation rule (31).

b) Offspring boundary derivation. Referring to (32), the OB is derived by the points on the Or.

These five stages determine the complete TDSSB, which will be validated in the next section.

4. Case studies

4.1. System description and parameter values

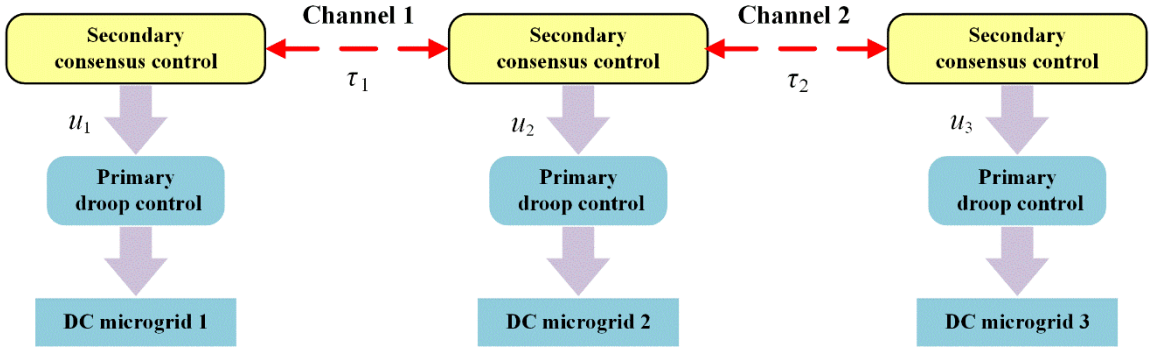

Fig. 4. The DC microgrid cluster with three DC microgrids.

For the TDSSB determination and the stability analysis, a DC microgrid cluster in Fig. 4 is employed as a demonstration. The system parameters are displayed in Table 1. The low voltage level 400V and the line résistance 0.05Ω are set for DC microgrids. The droop gain M_k represents the power-sharing ratio among the different DC microgrids. The identical power allocation is adopted in this study. The ability of voltage restoration is reflected by the integral gain α_k. The voltage comparison weight w_{1k} indicates the receiver of the voltage deviation information. The second DC microgrid is set as the receiver here. The consensus comparison weight w_{2k} indicates the collaborators in this cluster. During this illustration, all the DC microgrids would collaborate to guarantee the cluster stability. The equivalent load resistance of the DC microgrid cluster is set as 16Ω. It can be seen from Fig. 4 that two communication channels are considered in this cluster, which induces the time delays τ_1 and τ_2, respectively.

Table 1. System parameters.

Parameter	Symbol	DC microgrid 1	DC microgrid 2	DC microgrid 3
Nominal voltage	V^* (V)	400	400	400
Line resistance	R_k (Ω)	0.05	0.05	0.05
Droop gain	M_k	1	1	1
Integral gain	α_k	10	10	10
Voltage comparison weight	w_{1k}	0	1	0
Consensus comparison weight	w_{2k}	1	1	1

According to the communication network in Fig. 4, the adjacency matrix of the DC microgrid cluster is

$$\boldsymbol{A} = \begin{bmatrix} 0 & 1 & 0 \\ 1 & 0 & 1 \\ 0 & 1 & 0 \end{bmatrix} \tag{33}$$

To illustrate the TDSSB of the DC microgrid cluster with the distributed control framework, three scenarios are considered and investigated.

Scenario 1 (Non-delay scenario): the time delays in the Channel 1 and Channel 2 of the DC microgrid cluster are assumed to be 0, i.e., $\tau_1 = \tau_2 = 0$.

Scenario 2 (Single-delay scenario): the time delays in the Channel 1 and Channel 2 of the DC microgrid cluster are the identical, i.e., $\tau_1 = \tau_2 = \tau$.

Scenario 3 (Multiple-delay scenario): the time delays in the Channel 1 and Channel 2 of the DC microgrid cluster are different from each other, i.e., $\tau_1 \neq \tau_2$.

The mathematical simulations are implemented using Matlab 2015b. The computational platform is on an Intel(R) Core(TM) i3 2.53GHz personal computer with 6G memory.

4.2. Non-delay scenario

In the non-delay scenario, the time-delay model is reduced to a conventional linear model. As $\tau_1 = \tau_2 = 0$, the system dynamic is represented by a non-delay matrix $\tilde{\boldsymbol{A}}_0$

$$\tilde{\boldsymbol{A}}_0 = \begin{bmatrix} -10 & 10 & 0 \\ 6.738 & -23.262 & 6.738 \\ 0 & 10 & -10 \end{bmatrix} \tag{34}$$

The eigenvalues of $\tilde{\boldsymbol{A}}_0$ are listed in Table 2. As shown in Table 2, the three eigenvalues λ_1, λ_2, λ_3 of the DC microgrid cluster are negative real values. Therefore, the cluster is stable under the external disturbances. Besides, the system presents no oscillations as all the eigenvalues are real.

Table 2. The eigenvalues of the non-delay scenario.

Name	Symbol	Value
Eigenvalue 1	λ_1	-30
Eigenvalue 2	λ_2	-10
Eigenvalue 3	λ_3	-3.262

The DC bus variation is shown in Fig. 5 triggering a small voltage disturbance at t=5s. According to the bus curve in Fig. 5, the system voltage of the DC microgrid cluster can be effectually protected by the distributed control framework. During 0s-5s, v_{DC} operates stably at 400V. When the disturbance occurs at 5s, the DC bus voltage is quickly restored from 399.9V to 400V within 1.5s. It is also clear that the v_{DC} is monotonously recovered without any oscillations after the voltage drop. Hence, the cluster stability is well guaranteed in the non-delay scenario.

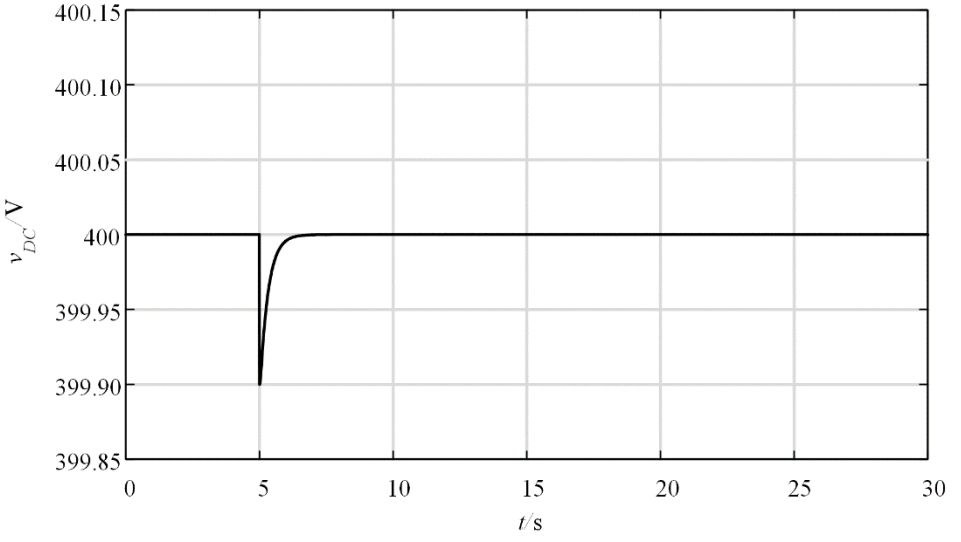

Fig. 5. DC bus voltage variation in the non-delay scenario.

4.3. Single-delay scenario

During the secondary consensus control, the control signals of neighboring DC microgrids are compared to restore the voltage maintaining the power assignment. For the comparison with the non-delay scenario, the TDSSB with the identical delay value is first analysed by the proposed method in Section 3. The implementation process is illustrated as follows.

Stage 1: System initialization.

Setting the derivation number j_p=8. The non-delay and time-delay coefficients in (16) are as follows

$$\bar{\boldsymbol{A}}_0 = \begin{bmatrix} -10 & 0 & 0 \\ -3.26 & -23.26 & -3.26 \\ 0 & 0 & -10 \end{bmatrix}, \ \bar{\boldsymbol{A}}_\tau = \begin{bmatrix} 0 & 10 & 0 \\ 10 & 0 & 10 \\ 0 & 10 & 0 \end{bmatrix} \tag{35}$$

The matrix $\tilde{\boldsymbol{A}}_0$ in the non-delay scenario has been separated into $\bar{\boldsymbol{A}}_0$ and $\bar{\boldsymbol{A}}_\tau$ in (35). The eigenvalues of these two matrices are recorded in Table 3.

Table 3. The eigenvalues of the non-delay and time-delay coefficients.

Coefficients	Eigenvalue 1	Eigenvalue 2	Eigenvalue 3
$\bar{\boldsymbol{A}}_0$	-23.262	-10	-10
$\bar{\boldsymbol{A}}_\tau$	-14.142	0	14.142

Although a time-delay coefficient has been extracted from $\tilde{\boldsymbol{A}}_0$, the eigenvalues of these two matrices

are still real as shown in Table 3. Different from the non-delay scenario, the separated $\bar{\boldsymbol{A}}_\tau$ has an unstable eigenvalue 14.142 and an eigenvalue 0, which forms the coefficient of the time-delay part.

Stage 2: Space transformation.

a) Space mapping. Through the substitution of $v = \tau\omega_c$, the characteristic equation is transformed to the spectral delay space

$$\mathrm{CE}(\omega_c, v) = \det\left(i\omega_c \boldsymbol{I}_{3\times3} - \bar{\boldsymbol{A}}_0 - \bar{\boldsymbol{A}}_\tau e^{-iv}\right) \tag{36}$$

The mapped (36) in the spectral delay space provides a simple approach to cope with the characteristic equation. Combing the two variables τ and ω_c into the variable *v*, the difficulty in determining TDSSB has been eliminated.

b) Equation rationalization. In order to eliminate the transcendental term e^{-iv}, (36) is rewritten via the half-angle tangent substitution

$$\mathrm{CE}(\omega_c, z) = \det\left[i\omega_c \boldsymbol{I}_{3\times3} - \bar{\boldsymbol{A}}_0 - \bar{\boldsymbol{A}}_\tau\left(\frac{1-z^2}{1+z^2} - i\frac{2z}{1+z^2}\right)\right] \tag{37}$$

It can be seen from (37) that the exponential component has vanished. On the basis of the rationalized equation, the time-delay problem has been simplified to a polynomial one.

c) Resultant formation. With the real-part coefficients $r_3(z)$, $r_2(z)$, $r_1(z)$, $r_0(z)$ and the imaginary-part coefficients $i_3(z)$, $i_2(z)$, $i_1(z)$, $i_0(z)$ of (37), the corresponding Sylvester resultant $\boldsymbol{M}$ is constructed

$$\boldsymbol{M} = \begin{vmatrix} r_3(z) & r_2(z) & r_1(z) & r_0(z) & 0 & 0 \\ 0 & r_3(z) & r_2(z) & r_1(z) & r_0(z) & 0 \\ 0 & 0 & r_3(z) & r_2(z) & r_1(z) & r_0(z) \\ i_3(z) & i_2(z) & i_1(z) & i_0(z) & 0 & 0 \\ 0 & i_3(z) & i_2(z) & i_1(z) & i_0(z) & 0 \\ 0 & 0 & i_3(z) & i_2(z) & i_1(z) & i_0(z) \end{vmatrix} \tag{38}$$

The matrix in (38) has the dimension of 6×6, which provides an effective tool to decouple the variables ω_c and *z*. For different imaginary roots of the characteristic equation, the real and the imaginary parts must be 0 simultaneously, which makes a zero resultant $\boldsymbol{M}$.

Stage 3: Spectral boundary sketch.

a) Kernel reflection search. According to the relationship between *z* and *v*, the variable *z* in (38) is replaced with *v*. The minimum interval (0, 2π) in the spectral delay space is evenly scanned to find out the critical point $v_{Kr} = 2.78$. Since there is only one critical point in the range of (0, 2π) for the single-delay system, this point constitutes the Kr in the spectral delay space.

b) Offspring reflection derivation. With the Kr and the derivation rule in (29), Ors are plotted in Fig. 6.

It can be seen from Fig. 6 that there are one Kr point and nine Or points in the interval of (0, 18π). With the derivation number j_p, 8 black points are found out within (2π, 18π), which are all associated with the same crossing root.

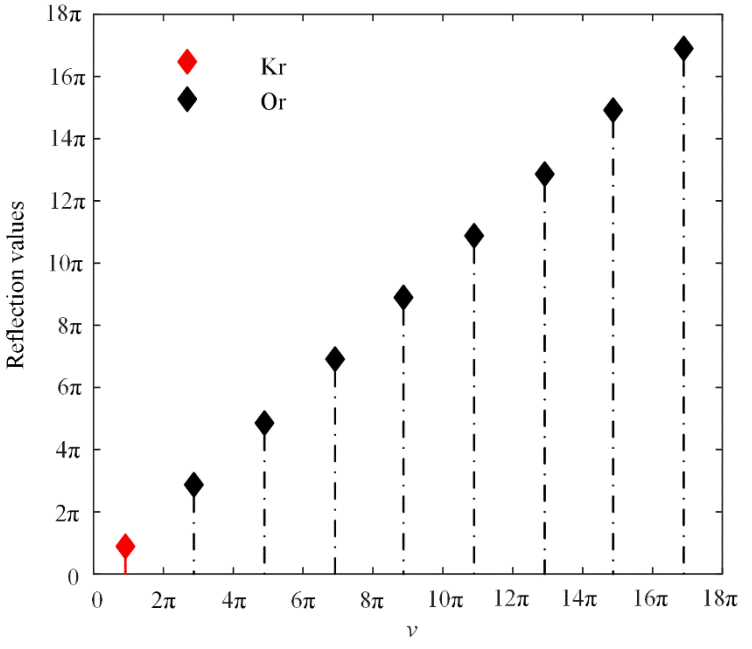

Fig. 6. The reflection values in the spectral delay space.

Stage 4: Crossing root calculation. According to the only point $v_{Kr} = 2.78$ of the Kr, the crossing root $i\omega_c = 4.67i$ is obtained solving the characteristic equation (30). This intriguing result indicates that the characteristic roots of the DC microgrid cluster periodically cross the imaginary axis at only two conjugate points $\pm 4.67i$. The corresponding oscillating frequency is 0.74Hz. During the growing of v in the spectral delay space, the stability switching times can be counted by $2(j_p + 1)$.

Stage 5: TDSSB determination.

a) Space back-mapping. With the inverse transformation rule, the KB point of the DC microgrid cluster is calculated in the time-delay space as

$$\tau_{KB} = v_{KB} / \omega_c = 0.59\text{s} \tag{39}$$

b) Offspring boundary derivation. Because there exists only one essential ω_c value, the OB points are evenly located along the time-delay axis. The coordinates of KB and the derived OB are listed in Table 4.

Table 4. The coordinates of TDSSB in the time-delay space.

	KB	OB 1	OB 2	OB 3	OB 4	OB 5	OB 6	OB 7	OB 8
τ_1	0.59	1.94	3.28	4.63	5.97	7.32	8.66	10.00	11.35
τ_2	0.59	1.94	3.28	4.63	5.97	7.32	8.66	10.00	11.35

The uniform difference for the distance between neighboring points is 1.90s in Table 4. Since 0.59s is the minimum time-delay value of the determined TDSSB, the DC voltage variation under $\tau = 0.59$s is shown in Fig. 7 to verify the proposed method.

When the value of the time delay increases, the oscillations of the DC bus become larger in magnitude from Fig. 7. Compared with the smooth curve in Fig. 5 for the non-delay scenario, the monotonous voltage variation has been broken by the delayed control signals. If τ is smaller than the minimum value of TDSSB, i.e., 0.59s, the voltage oscillation will fade with the elapse of time. Once the time delay

reaches the 0.59s, the equal amplitude oscillation will happen, which means that the system damping has disappeared due to the delay. The DC microgrid cluster will then switch to an unstable state beyond that point. For the cluster stability, the delay value should be smaller than 0.59s in this scenario.

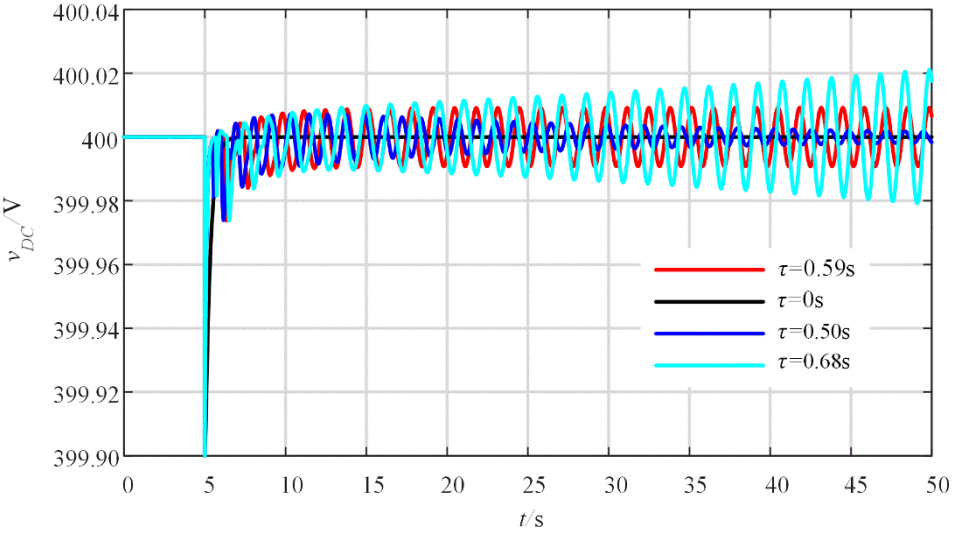

Fig. 7. DC bus voltage variations under different time-delay values.

4.4. Multiple-delay scenario

The investigation in Section 4.3 is based on the assumption that different communication channels are contaminated by an identical time delay, which is ideal for the real-time operation. In this section, the TDSSB is determined in a more general and realistic scenario considering different delay values.

Similar to the two scenarios before, the non-delay and time-delay coefficients are established

$$\boldsymbol{A}_0 = \begin{bmatrix} -10 & 0 & 0 \\ -3.26 & -23.26 & -3.26 \\ 0 & 0 & -10 \end{bmatrix},\ \boldsymbol{A}_{\tau 1} = \begin{bmatrix} 0 & 10 & 0 \\ 10 & 0 & 0 \\ 0 & 0 & 0 \end{bmatrix},\ \boldsymbol{A}_{\tau 2} = \begin{bmatrix} 0 & 0 & 0 \\ 0 & 0 & 10 \\ 0 & 10 & 0 \end{bmatrix} \tag{40}$$

The non-delay coefficients are the same as the ones in Section 4.3 and Section 4.4, while the time-delay coefficients are different. As the time delays in the Channel 1 and Channel 2 are different, the $\bar{\boldsymbol{A}}_\tau$ in the singular-delay scenario is separated into $\boldsymbol{A}_{\tau 1}$ and $\boldsymbol{A}_{\tau 2}$ in (40). According to the eigenvalues listed in Table 5, $\boldsymbol{A}_{\tau 1}$ and $\boldsymbol{A}_{\tau 2}$ have identical eigenvalues. But the spectral norms of these three matrices, i.e., their maximum eigenvalues here, satisfy $\|\boldsymbol{A}_{\tau 1}\|_2 = \|\boldsymbol{A}_{\tau 2}\|_2 < \|\bar{\boldsymbol{A}}_\tau\|_2$. It means that the individual coupling of $\boldsymbol{A}_{\tau 1}$ and τ_1 (or $\boldsymbol{A}_{\tau 2}$ and τ_2) is not as strong as that in the single-delay scenario.

Table 5. The eigenvalues of the non-delay and time-delay coefficients.

Coefficients	Eigenvalue 1	Eigenvalue 2	Eigenvalue 3
$\boldsymbol{A}_0$	-23.262	-10	-10
$\boldsymbol{A}_{\tau 1}$	-10	0	10
$\boldsymbol{A}_{\tau 2}$	-10	0	10

Following the same stages in Section 4.3, the Sylvester resultant is formed in the spectral delay space

$$\boldsymbol{M}=\begin{vmatrix} r_3(z_1,z_2) & r_2(z_1,z_2) & r_1(z_1,z_2) & r_0(z_1,z_2) & 0 & 0 \\ 0 & r_3(z_1,z_2) & r_2(z_1,z_2) & r_1(z_1,z_2) & r_0(z_1,z_2) & 0 \\ 0 & 0 & r_3(z_1,z_2) & r_2(z_1,z_2) & r_1(z_1,z_2) & r_0(z_1,z_2) \\ i_3(z_1,z_2) & i_2(z_1,z_2) & i_1(z_1,z_2) & i_0(z_1,z_2) & 0 & 0 \\ 0 & i_3(z_1,z_2) & i_2(z_1,z_2) & i_1(z_1,z_2) & i_0(z_1,z_2) & 0 \\ 0 & 0 & i_3(z_1,z_2) & i_2(z_1,z_2) & i_1(z_1,z_2) & i_0(z_1,z_2) \end{vmatrix} \tag{41}$$

where $r_3(z_1,z_2)$,…, $r_0(z_1,z_2)$ are the real-part coefficients, $i_3(z_1,z_2)$,…, $i_0(z_1,z_2)$ are the imaginary-part coefficients. With the solved 216 critical points making $\boldsymbol{M}$=0, the kernel reflection is assembled in Fig. 8.

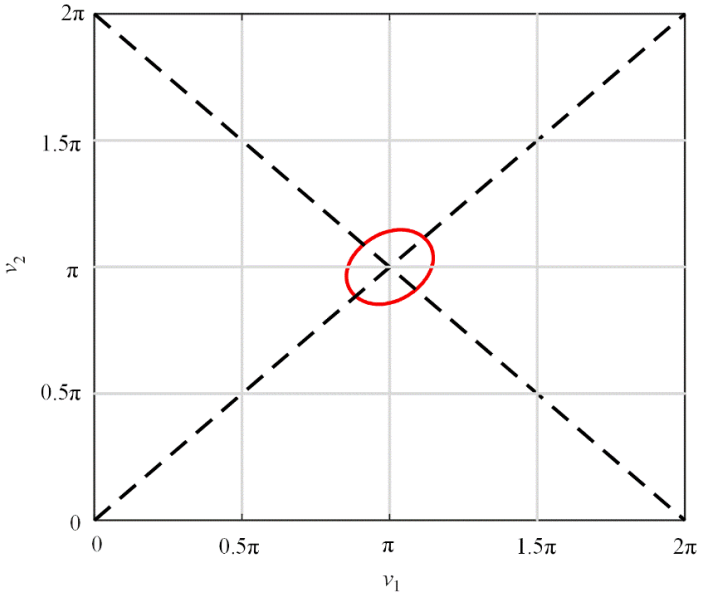

Fig. 8. The kernel reflection in the spectral delay space.

In Fig. 8, the red oval-like curve is the kernel reflection in the square region with the length 2π×2π. Crossing the two dashed diagonals, Kr locates at the regional center. Although the shape of Kr is not a circle, it can be seen that the boundary is symmetric with respect to the two diagonals of the square.

According to the period of 2π in the spectral delay space, the offspring reflections are derived by copying the Kr. The derived Ors along three directions are depicted in Fig. 9 (a)-(c).

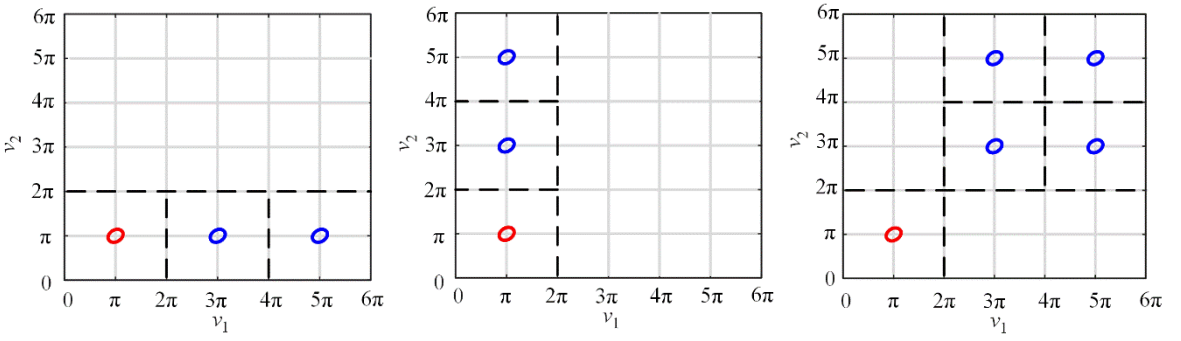

(a) Ors along the v_1 direction (b) Ors along the v_2 direction (c) Ors along the (v_1, v_2) direction

Fig. 9. The offspring reflections along three directions. (Red line: kernel reflection; blue line: offspring reflection)

From Fig. 9 (a)-(c), the mapped boundaries in the spectral delay space are shown clearly. Along the three directions, the Kr is translated to various Ors. The whole shape of all the boundaries is symmetrical along the diagonal. Even if an infinite number of offspring reflections can be derived with the 2π period, the corresponding purely imaginary roots remain unchanged. Therefore, all the $i\omega_c$ can be determined only by the kernel reflection.

Based on kernel reflection, all the crossing imaginary roots are calculated by the characteristic equation. The values of ω_c are shown in Fig. 10, where the horizontal ordinate n_S is the point indication on Kr.

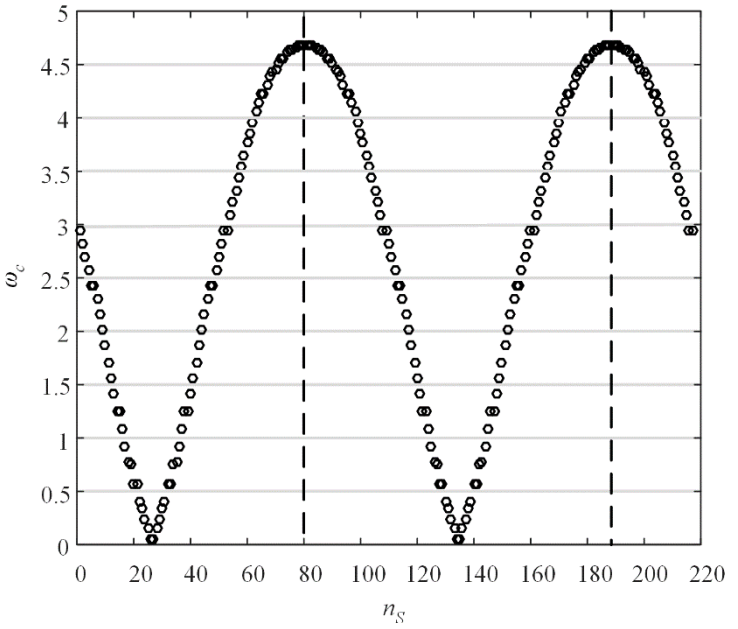

Fig. 10. The ω_c values of crossing root

As can be seen from Fig. 10, all the crossing roots are distributed within the range of [0.043, 4.67]. The radius of this range, i.e., 4.67, is just equal to the size of the crossing root in Section 4.3, which generates the maximum oscillating frequency 0.74Hz. The whole shape is similar to a sinusoidal (or cosinusoidal) function. Since all the imaginary roots exist in pairs, there are 108 pairs of $\pm\omega_c i$ for the DC microgrid cluster with the distributed control framework. According to the symmetry of Fig. 10 along the vertical dashed lines, the number of different pairs is only 54. The crossing root pair of the maximum amplitude is $\pm 4.68i$, while the pair of the minimum amplitude is $\pm 0.043i$.

The kernel boundary of the DC microgrid cluster is then back-mapped from the kernel reflection. As seen from Fig. 11, the KB is a radial curve in the time-delay space. The circular dot A (0.59, 0.59) is coincident with the TDSSB value determined in the single-delay scenario, which is the closest point to the origin. Since the smallest $\|\boldsymbol{\tau}\|_2$ causes the maximum oscillating frequency, this identical delay value in different channels should be strictly avoided. A1-A3 are three points close to KB as shown in Fig. 11. The voltage waveforms for these three points are shown in Fig. 12.

With the growing value of τ_2, A1-A3 crosses the kernel boundary vertically. The stability switching of the DC microgrid cluster is A2 with $\tau_1 = 3.00\text{s}$ and $\tau_2 = 2.50\text{s}$. As clearly seen from Fig. 12, DC microgrid cluster has switched its stability during the crossing process. An interesting finding in Fig. 11

and Fig. 12 is that the delay scenario of A1 (3.00, 2.00) is stable, which satisfies $\tau_1 \neq \tau_2$. Although the delay values in the two channels of A1 have already been much bigger than those of A, the cluster can still keep its stability. Hence, it is helpful for the system stability making the time-delay values different.

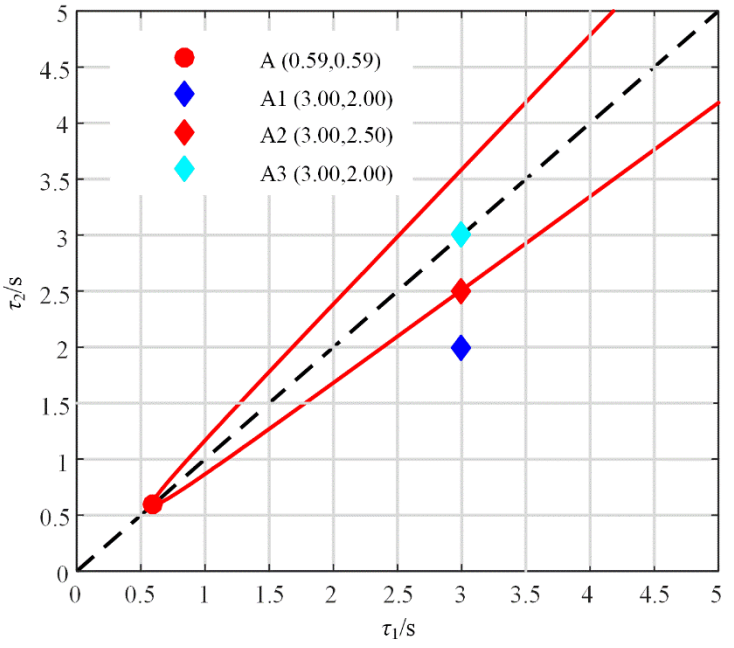

Fig. 11. The kernel boundary in the time-delay space.

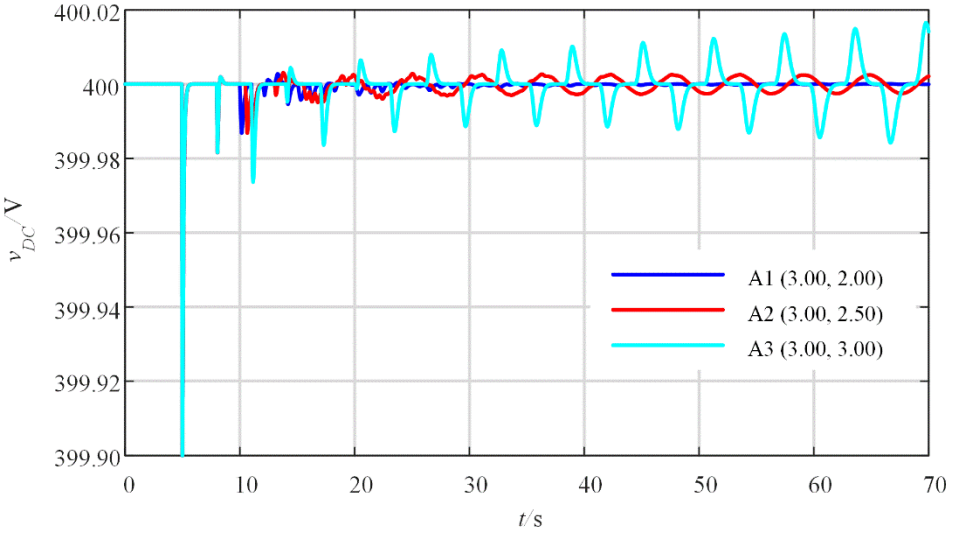

Fig. 12. The bus voltage variations at A1-A3.

In terms of the offspring boundary, the Ors in Fig. 9 are inversely reflected in the three directions likewise. According to the boundaries in Fig. 13, the whole delay space is separated into many regions, which presents a radial pattern. According to the continuity of the linear system [34], the stable region is continuous involving the origin, which is separated from the unstable region by the TDSSB. Even if an infinite number of offspring boundaries will continually reproduce along the three dimensions, there are still many stable areas between TDSSBs.

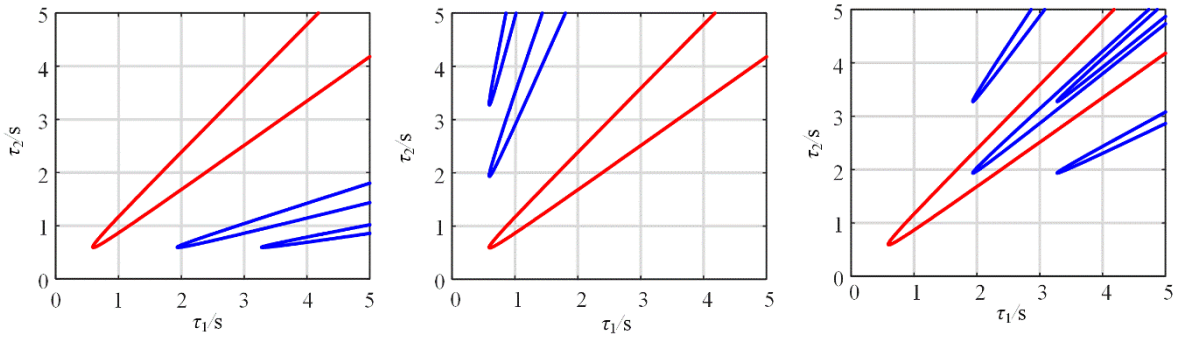

(a) OBs along the τ_1 direction (b) OBs along the τ_2 direction (c) OBs along the (τ_1 , τ_2) direction

Fig. 13. The offspring boundaries along three directions. (Red line: kernel boundary; blue line: offspring boundary)

For the presentation of the TDSSB panorama, all the boundaries in Fig. 13 (a)-(c) are gathered forming Fig. 14.

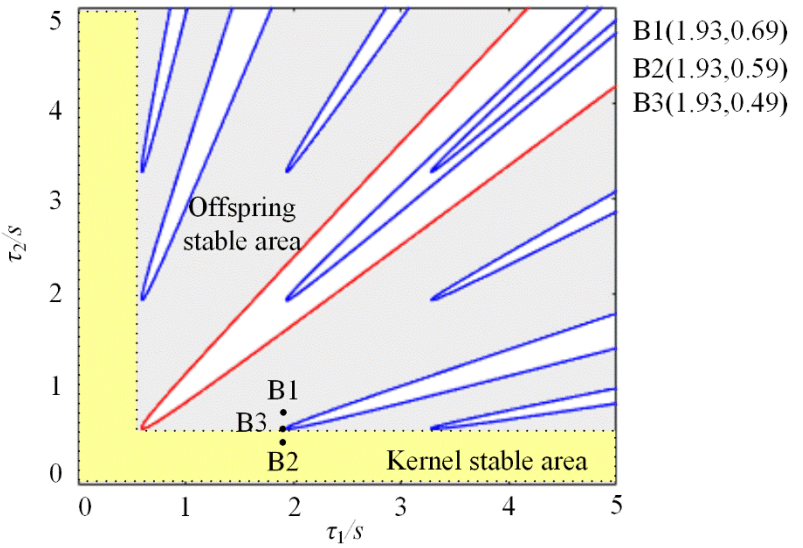

Fig. 14. The TDSSB of the DC microgrid cluster with the distributed control framework.

The benefits of Fig. 13 and Fig.14 to the practical microgrid deployment are in three aspects:

1) Impact visualization. The boundaries in Figure 13 and Figure 14 visualize the time-delay impact for the practical microgrid deployment. According to the distribution of TDSSB in the time-delay space, it can directly judge whether the current time delays can damage the system stability. Supposed the current time delays in Channel 1 and Channel 2 are both 1s, this delay point falls into the unstable area divided by the TDSSB. Hence, the operation in this time-delay state is harmful to the microgrid. In contrast, the microgrid cluster can operate stably with 1s delay in Channel 1 and 1.5s delay in Channel 2, hich locates in the stable area.

2) Stability guidance. Fig. 13 and Fig. 14 are beneficial to protect the practical microgrid deployment from the time-delay instability. According to the time-delay state in different communication channels, these two figures can conveniently provide the guidance strategy. For example, the current delay point is (1, 1) in the unstable area. Instead of maintaining two communication channels simultaneously, the system stability can be effectively enhanced decreasing one time-delay below 0.5s according to Figure 14.

3) Cluster design. On the basis of various requirements from the microgrid cluster, these two figures can be quickly re-plotted guiding the cluster design. Once the TDSSB is very near to the origin, the stability of deployed microgrids would be very sensitive to the time delay. Hence, the design of communication channel should be paid much effort satisfying the time-delay constraints provided by Figure 13 and 14.

The stable region in Fig. 14 can be further classified into two types:

1) Kernel stable area (yellow): This area is surrounded by the KB apex of TDSSB and the dotted line parallel to the delay axes. The apex of KB has the smallest $\|\boldsymbol{\tau}\|_2$ compared to the other points on the TDSSB. The kernel stable area has a regular shape along the axes. The stable points in this area have the same feature that at least one time-delay component is smaller than that of the KB apex.

2) Offspring stable area (cyan): This area is surrounded by all the edges of TDSSB. The edge of each boundary is made up of all the points on the TDSSB. The offspring stable area is an irregular shape encircles the kernel stable area. The stable points in this area have the same feature that they are not in the diagonal direction which indicates all the channel delays are identical.

Kernel stable area and offspring stable area make up the whole stable region for the microgrid cluster. With the TDSSB and the classified stable areas, two strategies can be comfortably proposed to enhance the cluster stability during the cluster design and the real-time operation.

1) Kernel strategy: The DC microgrid can tolerate the time-delay operation by the good maintenance of one communication channel. This strategy can be explained by the time-delay point B1 (1.93, 0.49) in the kernel stable area of Fig. 14. By the preservation of τ_2 in the Channel 2 smaller than 0.59s, the acceptable time-delay value of Channel 1 can be obviously extended along the τ_1 direction. The kernel strategy is helpful to guarantee the cluster stability without spending effort on all the communication channels. Setting a strict condition for one channel, the stability can be significantly improved.

2) Offspring strategy: The DC microgrid can tolerate the time-delay operation by the avoidance of the identical time-delay value. This strategy can be represented by the time-delay point B2 (1.93, 0.69) in the

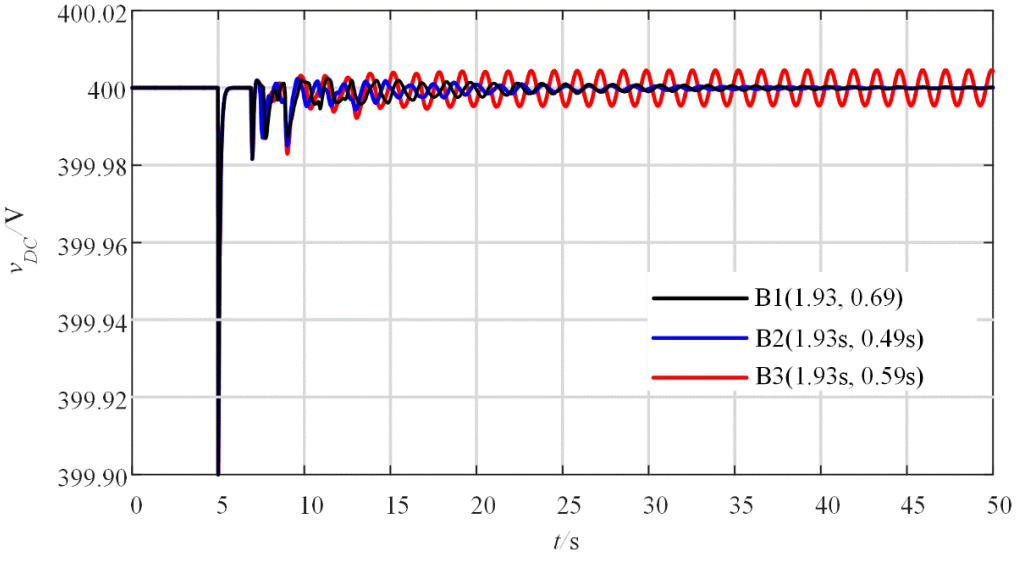

Fig. 15. The stability enhancement by the kernel and the offspring strategies.

stable area of Fig. 14. Although τ_1 in the Channel 1 is much larger than $\tau_2 = 0.69$s, the microgrid cluster can still work stably. The offspring strategy reveals that the non-uniform network is helpful to protect the system stability. The time-delay stability would be weak once all the time-delay components are the same.

These two strategies are demonstrated in Fig. 15. Under the time-delay scenarios at B1 (kernel strategy) and B2 (offspring strategy), the cluster voltage can effectively recover within 5s. Although the kernel and offspring strategies only make small changes to the time delay of Channel 2, the system stability has been significantly enhanced avoiding the oscillations at B3.

On the basis of Fig. 15, the oscillation comparisons of B1-B3 after *t*=10s are displayed in Table 6.

Table 6. Oscillation comparisons of B1-B3.

	B1	B2	B3
Maximum magnitude (10^{-3}V)	5.5	5.6	7.8
Occurrence time (s)	10.9s	12.9s	13.0s

Although the kernel strategy and the offspring strategy are both capable of the stability protection, there are still small differences between this two strategies in Table 6. The magnitude under B1 is the smallest among these three time-delay scenarios. Besides, the corresponding time is also the earliest, i.e., 10.9s. The cluster would experience the maximum oscillation almost 2s later at B2 and B3.

In order to indicate the accuracy of the proposed method, the two stability criteria based on the free-weighting matrix (FWM) [26] and the Jensen inequality (JI) [28] are employed for the following comparison.

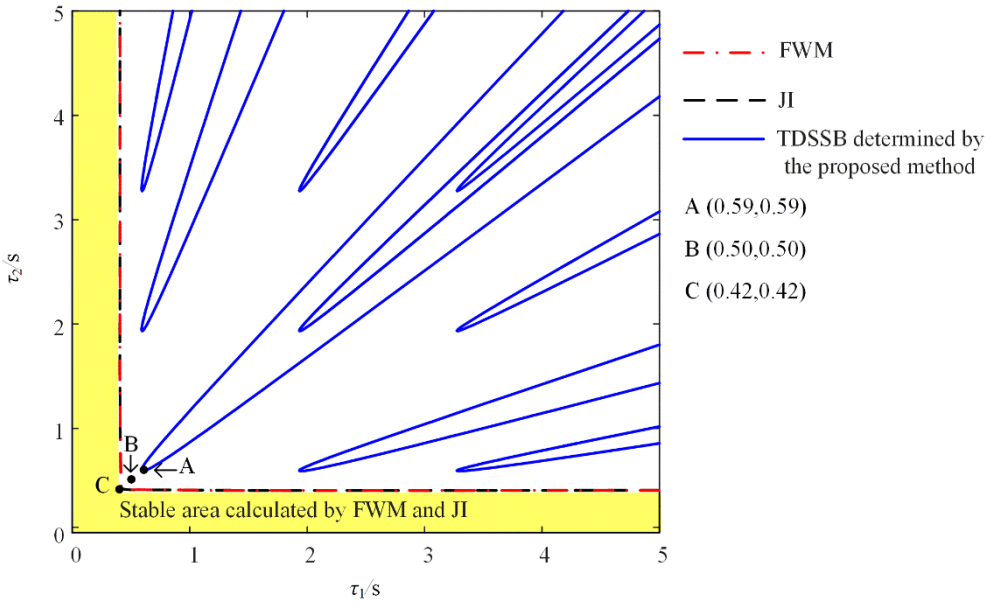

Fig. 16. The TDSSBs calculated by the three methods.

It can be seen from Fig. 16 that the TDSSBs calculated by the stability criteria based on FWM and JI are obviously conservative compared with the determined TDSSB in this paper. The boundaries calculated by FWM and JI are the same, which can only judge the yellow area as the stable area. As

shown in Fig. 16, the large stable area between the dashed line and the solid line will be regarded unstable by FWM and JI. However, the proposed method is able to provide the accurate TDSSB in the blue color. The voltage variations at A (0.59, 0.59), B (0.50, 0.50), and C (0.42, 0.42) are shown in Fig. 17.

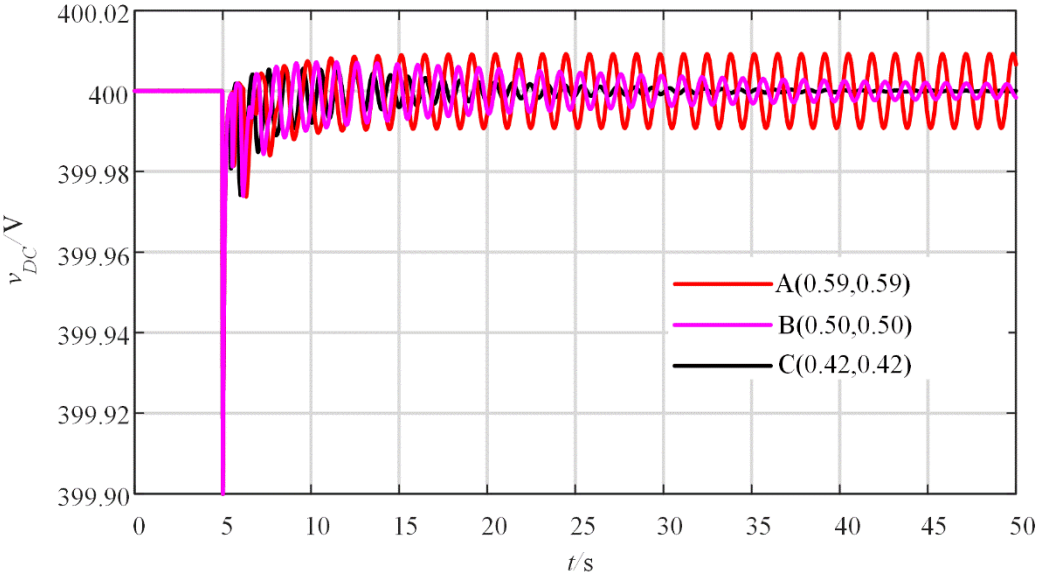

Fig. 17. DC bus voltage variations under different time-delay scenarios of A, B, and C

According to Fig. 17, the DC bus voltage recovers to its nominal value of 400V under the delay scenario of C which is on the calculated TDSSB via the FWM and JI methods. However, the system can still guarantee the stability with the increased delay at B. The equal amplitude oscillation will finally happen at A, which indicates the accurate boundary point with $\tau_1 = 0.59\text{s}$, $\tau_2 = 0.59\text{s}$. To quantitatively analyse the accuracy improvement in this work, the error index is defined as follows

$$\text{Error index} = \frac{\|\boldsymbol{\tau}_A\|_2 - \|\boldsymbol{\tau}_C\|_2}{\|\boldsymbol{\tau}_A\|_2} \times 100\% \tag{42}$$

where $\boldsymbol{\tau}_A$ denotes the point on the TDSSB nearest to the origin calculated by the proposed method, $\boldsymbol{\tau}_C$ denotes the point on the TDSSB nearest to the origin calculated by one method. The error indexes of these three methods are displayed in Table 7.

Table 7. Error indexes of three methods.

	The proposed method	FWM	JI
Error index (%)	0	28.81	28.81

It can be seen from Table 7 that the accuracy of the proposed method is notable. The error indexes of FWM and JI both reached 28.81%. Hence, the TDSSB determination result of the proposed method can provide the accurate time-delay stability information for the DC microgrid cluster.

5. Conclusion

This paper proposes to investigate the explicit time-delay stability for the DC microgrid cluster with the distributed control framework. Through the derived time-delay stability model and the defined time-delay stability switching boundary, the delay issue of the microgrid cluster is accurately examined. In order to determine the complete boundary composed of kernel boundary and offspring boundary, the spectral delay space is deployed to linearize the boundary derivation process. The main findings of this article are presented as follows.

- The time-delay stability switching boundary of the DC microgrid cluster exists, which is made up of the kernel and offspring boundaries;
- The proposed approach is effective to determine the accurate boundary for the DC microgrid cluster;
- The boundary in the time-delay space can be represented by a closed boundary in the spectral delay space;
- The time delay is disclosed as an oscillation source of the DC microgrid cluster;
- The determined boundary divides the stable area in the time-delay space into the kernel and offspring stable areas;
- The time-delay stability of the DC microgrid cluster can be enhanced by setting a strict constraint in one channel or adopting the non-uniform network.

On the basis of this work, we plan to study three major aspects in the future.

- Studying the reason for the existence of the time-delay stability switching boundary;
- Improving the approach efficiency through the reduction of the implementation stages;
- Extending the proposed modeling procedure and systemic analysis to design novel stability enhancement strategies.

Acknowledgments

This work was financially supported by the National High-tech R&D Program of China (2015AA050403) and the National Natural Science Foundation of China (U1766210, 51377117).

References

[1] Report on the government work of the People's Republic of China, 2018; <http://www.mod.gov.cn/top-news/2018-03/05/content_4805962.htm>
[2] Wang CS, Yan JY, Marnay C, Djilali N, Dahlquist E, Wu JZ, Jia HJ. Distributed energy and microgrids (DEM). Applied Energy 2018; **210**: 685-89.
[3] Meng LX, Shafiee Q, Trecate FG, Karimi H, Fulwani D, Lu XN, Guerrero JM. Review on control of DC microgrids and multiple microgrid clusters. IEEE J Emerg Sel Top Power Electron 2017; **5(3)**: 928-48.
[4] Lotfi H, Khodaei A. Hybrid AC/DC microgrid planning. Energy 2017; **118**: 37-46.
[5] Bullich-Massagué E, Díaz-González F, Aragüés-Peñalba M, Girbau-Llistuella F, Olivella-Rosell P, Sumper A. Microgrid clustering architectures. Applied Energy 2018; **212**: 340-61.
[6] Boroojeni K, Amini MH., Nejadpak A, Dragičević T, Iyengar SS, Blaabjerg F. A novel cloud-based platform for implementation of oblivious power routing for clusters of microgrids. IEEE Access 2017; **5**: 607-19.
[7] Amini MH, Boroojeni KG, Dragičević T, Nejadpak A, Iyengar SS, Blaabjerg F. A comprehensive cloud-based real-time simulation framework for oblivious power routing in clusters of dc microgrids. IEEE ICDCM, 2017: 270-73.
[8] Kolluri RR, Mareels I, Alpcan T, Brazil M, Hoog JD, Thomas DA. Power sharing in angle droop controlled microgrids. IEEE Trans Power Sys 2017; **32(6)**: 4743–51.
[9] Moayedi S, Davoudi A. Distributed tertiary control of DC microgrid cluster. IEEE Trans Power Electron 2016; **31(2)**: 1717-

33.
[10] Almada JB, Leão RPS, Sampaio RF, Barroso GC. A centralized and heuristic approach for energy management of an AC microgrid. Renew Sustain Energy Rev 2016, **60**: 1396-404
[11] Bahrami S, Amini MH. A decentralized trading algorithm for an electricity market with generation uncertainty. Applied Energy 2018; **218**: 520-32.
[12] Pasha AM, Zeineldin HH, Al-Sumaiti AS, El-Moursi MS, El Sadaany EF. Conservation voltage reduction for autonomous microgrids based on V–I droop characteristics. IEEE Trans Sustain Energy 2017, **8(3)**: 1076-85.
[13] Fani B, Zandi Farshad, Karami-Horestani A. An enhanced decentralized reactive power sharing strategy for inverter-based microgrid. Electric Power Energy Syst 2017; **98**: 531–42.
[14] Riverso S, Tucci M, Vasquez JC, Guerrero JM, Ferrari-Trecate G. Stabilizing plug-and-play regulators and secondary coordinated control for AC islanded microgrids with bus-connected topology. Applied Energy 2018; **210**: 914-24.
[15] Bünning F, Sangi R, Müller D. A Modelica library for the agent-based control of building energy systems. Applied Energy 2018; **193**: 52-59.
[16] Xydas E, Marmaras C, Cipcigan LM. A multi-agent based scheduling algorithm for adaptive electric vehicles charging. Applied Energy 2016; **177**: 354-65.
[17] Guo FH, Wen CY, Miao JF, Song YD. Distributed secondary voltage and frequency restoration control of droop-controlled inverter-based microgrids. IEEE Trans Ind Electron 2015; **62(7)**: 4355–64.
[18] Mohammadi FD, Vanashi HK, Feliachi A. State-space modeling, analysis, and distributed secondary frequency control of isolated microgrids. IEEE Trans Energy Convers 2018; **33(1)**: 155–65.
[19] Mo HD, Li YF, Zio E. A system-of-systems framework for the reliability analysis of distributed generation systems accounting for the impact of degraded communication networks. Applied Energy 2016; **183**: 805-22.
[20] Behjati H, Davoudi A, Lewis F. Modular DC–DC converters on graphs: cooperative control. IEEE Trans Power Electron 2014; **29(12)**: 6725–41.
[21] Ren LY, Qin YY, Li Y, Zhang P, Wang B, Luh PB, Song H, Orekan T, Gong T. Enabling resilient distributed power sharing in networked microgrids through software defined networking. Applied Energy 2018; **210**: 1251-65.
[22] Jia HJ, Li XM, Mu YF, Xu C, Jiang YL, Yu XD, Wu JZ, Dong CY. Coordinated control for EV aggregators and power plants in frequency regulation considering time-varying delays. Applied Energy 2018; **210**: 1363-76.
[23] Lai JG, Zhou H, Lu XQ, Yu XH, Hu WS. Droop-based distributed cooperative control for microgrids with time-varying delays. IEEE Trans Smart Grid 2016; **7(4)**: 1775–89.
[24] Ahmadi A, Aldeen M. An LMI approach to the design of robust delay-dependent overlapping load frequency control of uncertain power systems. Int J Electr Power Energy Syst 2016; **81**: 48-63.
[25] Gao QB, Kammer AS, Zalluhoglu U, Olgac N. Critical effects of the polarity change in delayed states within an LTI dynamics with multiple delays. IEEE Trans Automat Control 2015; **60(11)**: 3018-22.
[26] Dong CY, Jia HJ, Jiang T, Bai LQ, Hu QR, Wang L, Jiang YL. Effective method to determine time-delay stability margin and its application to power systems. IET Gener Transm Distrib 2017; **11(7)**: 1661-70.
[27] Medvedeva IV, Zhabko AP. Synthesis of Razumikhin and Lyapunov–Krasovskii approaches to stability analysis of time-delay systems. Automatica 2015; **51**: 372–77.
[28] Zhang CK, He Y, Jiang L, Wu M. Notes on stability of time-delay systems: bounding inequalities and augmented Lyapunov-Krasovskii functionals. IEEE Trans Automat Control 2017; **62(10)**: 5331-36.
[29] Milano F. Small-signal stability analysis of large power systems with inclusion of multiple delays. IEEE Trans Power Sys 2016; **31**: 3257–66.
[30] Gu K, Kharitonov V L, Chen J. Stability of time-delay systems, Springer Birkhauser, 2003.
[31] Gao Q, Olgac N. Bounds of imaginary spectra of LTI systems in the domain of two of the multiple time delays. Automatica 2016; **72**: 235–41.
[32] Feldmann P, Rohrer RA. Proof of the number of independent Kirchhoff equations in an electrical circuit. IEEE Trans Circuit Sys 1991; **38(7)**: 81–84.
[33] Petkov PH, Christov ND, Konstantinov MM. Computational methods for linear control systems. Automatica 1993; **29(2)**: 568–70.
[34] Hale JK, Theory of functional differential equations, Springer-Verlag, New York, 1977.